

University of Nevada, Reno

**Analyzing variation in snow albedo across spatial scales of observation in the  
Alaskan boreal forest**

A thesis submitted in partial fulfillment of the  
requirements for the degree of Master of Science in  
Hydrogeology

By

Allyson Fitts

Dr. Anne Nolin/Thesis Advisor

August, 2024



THE GRADUATE SCHOOL

We recommend that the thesis  
prepared under our supervision by

**ALLYSON FITTS**

entitled

**Analyzing variation in snow albedo across spatial scales of  
observation in the Alaskan boreal forest**

be accepted in partial fulfillment of the  
requirements for the degree of

**MASTER OF SCIENCE**

Anne Nolin, Ph.D.  
*Advisor*

Ken Nussear, Ph.D.  
*Committee Member*

Kelly Gleason, Ph.D.  
*Committee Member*

Carlos Ramirez-Reyes, Ph.D.  
*Graduate School Representative*

Markus Kemmelmeier, Ph.D., Dean  
*Graduate School*

August, 2024

## ABSTRACT

Snow albedo plays a critical role in the Earth's energy balance due to its high reflectivity in the visible wavelengths. On average, more than 50% of the land area above 20° North latitude is snow covered by December. In a warming climate where temperatures are estimated to rise and less precipitation will fall as snow in high latitude regions, it is crucial to understand variation in snow albedo across changing spatial scales. The albedo of snow is a primary control on the timing and rate of snowmelt and is affected by grain size and light absorbing impurities, such as black carbon shed from burned trees after a wildfire. Like the western United States, the boreal forests in Alaska are experiencing an increase in wildfire activity, drastically altering both the regional and global energy balance. After a wildfire, light absorbing particles such as black carbon and woody debris are deposited on the snow surface. These particles darken the snow surface, decreasing snow albedo and increasing the shortwave energy absorbed at the surface. From a landscape perspective, removing the dark forest canopy cover by fires increases the landscape albedo, yet the snow albedo is decreased. This research strives to untangle the paradox between the point and landscape scale across varying vegetation cover. To do so, we compare multispectral and hyperspectral remote sensing instrumentation across scales of observation from ground-based transects to airborne and satellite-based measurements. Using airborne data from Airborne Visible/Infrared Imaging Spectrometer (AVIRIS-NG), we conducted a spectral unmixing analysis to characterize the fraction of snow across transects. Assuming ground measurements are entirely snow, we compared field spectrometer measurements to

airborne and satellite reflectance data, which have a coarser spatial resolution. We computed the difference in reflectance values for ground-based vs. airborne and ground-based vs. satellite data. Results show that there is a linear relationship between reflectance differences and the fraction of snow cover in a mixed pixel. As the fraction of snow cover in a pixel increases, the cross-scale reflectance differences decrease in a linear manner. This means that if we know the snow fraction in a pixel, and we have measured the reflectance at one scale, then we can linearly interpolate to estimate the reflectance that would be measured at a finer or coarser scale. Moreover, if we can assume that albedo generally tracks with reflectance, we can estimate landscape albedo at different spatial scales. We conclude that the land cover classification and spatial scale of observation must be considered when estimating snow and landscape albedo. Instruments tend to agree well in snow covered, open areas compared to forested areas. Fine resolution airborne data, such as AVIRIS-NG, tends to agree with ground observations in open and burned areas. We encourage the snow remote sensing community to consider instrument optics and their spectral, spatial and temporal resolution as it relates to area classification when utilizing snow reflectance data products.

## ACKNOWLEDGEMENTS

I would like to thank Dr. Anne Nolin, my thesis advisor, for the incredible opportunity to pursue a master's degree at the University of Nevada, Reno. Thank you for your continued support and sharing your wealth of knowledge with me over the past two years. I am inspired by your dedication to your students and research, and I am forever grateful to have worked alongside you.

Dr. Ken Nussear, thank you for guiding me through my data analysis, willingness to pivot when field work obstacles arise, and constant positivity and reassurance throughout the research process. Dr. Kelly Gleason, thank you for sharing your snow hydrology and statistical expertise, as well as your support in the field. Dr. Carlos Ramirez-Reyes, thank you for always being willing to help me troubleshoot in R and ENVI and providing critical statistical insight.

Special thanks to the Computational Mountain Studies Lab. Dr. Jack Tarricone, thank you for your constant support and guidance with navigating graduate school, data processing and analysis and my career. Hannah Van Dusen, thank you for helping me through coursework and working through graduate school challenges. Griffin Shelor, thank you for the company in the office.

Thank you to the Graduate Program of Hydrologic Sciences for helping me find my community in Reno. I would like to thank Cara Sullivan, Dylen Swan, Hannah Lukaski, and Alyssa Radakovich for always supporting me.

Thank you to the snow hydrology community for constantly inspiring and encouraging me to become a better scientist.

To my family and friends, thank you for the unconditional encouragement and support from Day 1. You all are my backbone.

## TABLE OF CONTENTS

ABSTRACT .....	i
ACKNOWLEDGEMENTS.....	iii
TABLE OF CONTENTS.....	v
LIST OF TABLES .....	vii
LIST OF FIGURES .....	ix
LIST OF EQUATIONS .....	xi
1. INTRODUCTION.....	1
1.1. Significance .....	1
1.2. Motivation .....	2
1.3. Research Objectives .....	3
2. BACKGROUND AND PREVIOUS WORK .....	4
2.1. Changing Snow Conditions in a Warming Climate .....	4
2.2. Wildfire Behavior .....	5
2.3. Snow Albedo.....	5
2.4. Snow Grain Size.....	6
2.5. Post-Fire Effects on Snow Albedo Across Spatial Scales.....	6
2.6. Reflectance vs. Albedo.....	9
2.7. Snow Albedo and Reflectance Measurement Instrumentation and Models .....	10
2.7.1. Field Spectrometer.....	10
2.7.2. AVIRIS-NG.....	11
2.7.3. Landsat 8-9 OLI Surface Reflectance.....	12
i. Snow, Ice and Aerosol Radiative (SNICAR) model .....	12
3. RESEARCH METHODS.....	13
3.1. Introduction to Snow Albedo Field Campaigns: 2023 and 2024.....	13
3.1.1. SnowEx Snow Albedo Campaign 2023.....	14
3.1.2. Terrestrial Hydrology Program - Snow Albedo Campaign 2024.....	14
3.2. Description of Study Areas.....	15
3.3. Field Spectrometer Measurements .....	17
3.3.1. Field Sampling.....	17
3.3.2. Data Post-Processing .....	19
3.4. AVIRIS-NG.....	20

3.5.	Geolocation Accuracy .....	23
3.6.	Landsat 8-9 OLI.....	23
3.7.	Statistical Analyses.....	25
3.7.1.	Reflectance Comparisons.....	25
3.7.2.	Scaling Relationships .....	26
3.8.	Estimating Effective Grain Radius with SNICAR.....	26
3.8.1.	Calculating Scaled Band Area and Effective Grain Radius for Ground-based and Airborne Measurements .....	30
3.9.	Open, Old Burn Characterization.....	32
4.	RESULTS.....	33
4.1.	Statistical Analyses.....	34
4.1.1.	Reflectance Comparisons.....	34
4.1.2.	Scaling Relationships .....	37
4.2.	AVIRIS-NG Scaled Band Area and SNOTEL relationship.....	40
4.3.	Linear Spectral Unmixing .....	41
4.4.	Spectral Library.....	42
5.	DISCUSSION.....	43
5.1.	Overview of Key Findings.....	43
5.1.1.	Linear Scaling Relationships.....	43
5.1.2.	Reflectance Comparison by Instrument, Spectral Regions, and Site Type .....	44
5.1.3.	Comparison of Effective Grain Radii Across Scales .....	45
5.1.4.	Creamer’s Field AVIRIS-NG Scaled Band Area and SNOTEL relationship .....	45
5.2.	Error Analysis .....	45
5.2.1.	Sources of Possible Measurement Error.....	45
6.	CONCLUSIONS.....	48
	REFERENCES .....	51
	SUPPLEMENTAL MATERIAL .....	56
	DATA AND CODE AVAILABILITY .....	56
	SPECTRAL LIBRARY.....	56
	TABLES .....	60
	FIGURES.....	63

## LIST OF TABLES

**Table 1.** *Summary table of measured reflectance quantities discussed in Schaepman-Strub et al. (2006) and applied in this research.*

**Table 2.** *SnowEx Snow Albedo Alaska 2023 campaign transect characterization by location, number, site type (burn, forest, or open), dominant vegetation type, average elevation, topographic setting, and affiliation (Alaska Department of Fish and Game (ASFG), National Ecological Observation Network (NEON), NASA Arctic Boreal Vulnerability Experiment (ABOVE), and/or Long Term Ecological Research (LTER)).*

**Table 3.** *Spectral band description and wavelength range of Landsat 8-9 Operational Land Imager (OLI) Collection Surface Reflectance data.*

**Table 4.** *Spectral regions with associated spectral range (1 nm) and AVIRIS-NG channels (5 nm intervals)*

**Table 5.** *Parameters and corresponding values selected for SNICAR-Adv3: Online Snow Albedo Simulator.*

**Table 6.** *Calculated scaled band area and estimated snow grain radius for average snow reflectance from field spectrometer measurements. Transects were chosen if they have coincident airborne measurements. Spectra of field spectrometer and SNICAR modeled spectra are provided in Figure S.2.*

**Table 7.** *Calculated scaled band area and estimated snow grain radius for average snow reflectance from AVIRIS-NG data. Transects were chosen if they have coincident ground measurements. Spectra of AVIRIS-NG and SNICAR modeled spectra are provided in Figure S.3.*

**Table 8.** *Results for Games Howell statistical test, comparing instruments (AVIRIS-NG and field spectrometer) across spectral subsets and site types. All comparisons show statistically significant differences.*

**Table 9.** *The difference in median of AVIRIS-NG and the field spectrometer grouped by spectral region and site type. Data visualized in Figure 6.*

**Table 10.** *Summary statistics associated with box and whisker plots (Figure 7). Comparison of individual open (historic burn) transect broken down by instrument and spectral region. The instruments include a field spectrometer (FS) and AVIRIS-NG (AV).*

**Table 11.** *The average difference between Landsat 8-9 OLI and coincident field spectrometer (aggregated to Landsat 8-9 OLI spectral range) by site type.*

**Table 12.** *Results from Linear Spectral Unmixing analysis on AVIRIS-NG scenes with coincident ground observations. The table is grouped by transect characterization (Burn, Forest, Open). The data presented are the normalized geometric mean of pixels containing snow or vegetation. The RMS error (RMSE) describes how representative the end members are of the AVIRIS-NG pixels.*

SUPPLEMENTARY MATERIAL

**Table S.1.** Average measured reflectance values for ground-based field spectrometer and Landsat 8-9. Field spectrometer spectral bands were aggregated to Landsat 8-9 spectral resolution. Measurements are shown only for near-coincident ground-based measurements and Landsat overpasses occurred ( $\pm 1$  day).

**Table S.2.** Reference table including location input to NOAA Solar Position Calculator and estimates solar zenith angle.

**Table S.3.** Look up table using SNICAR modeled snow spectra with parameters previously discussed at various effective grain radii. SBA estimated to 3<sup>rd</sup> decimal place.

## LIST OF FIGURES

**Figure 1.** The post-fire effect of light absorbing particles (LAPs) on snow covered forested areas across forest densities from varying scales of observation. Developed by A. Nolin.

**Figure 2.** Map overview of 2023 campaign study area, where A) general location of campaign in Alaska, B) proximity of sites to one another, C) Creamer's Field site with single transect, D) Delta Junction site with three transects, and E) CPCRW site with three ranging transects, including the 2021 Haystack Fire burned area.

**Figure 3.** Spectral profile of snow and vegetation endmembers selected from within an individual AVIRIS-NG for the linear spectral unmixing analysis.

**Figure 4.** Scaled band area method to estimate effective grain radius, where the dashed red line is the continuum and solid blue line is reflectance. Spectra represents SNICAR output of an effective grain radius of 850  $\mu\text{m}$ .

**Figure 5.** Modeled relationship between calculated scaled band area and effect grain radius (left) and relationship between broadband albedo and effective grain radius (right). Data produced using the SNICAR-ADv3: Online Snow Albedo Simulator.

**Figure 6.** Box and Whisker plots comparing average reflectance between instruments grouped by site type and spectral region. In legend, "AVIRIS" is referring to AVIRIS-NG, and "FieldSpec" is referring to field spectrometer measurements.

**Figure 7.** Box and Whisker plots comparing average reflectance in the visible and near-infrared wavelengths by instrument across a transect characterized as open. Effective Grain Radius estimated using SNICAR modeled relationship.

**Figure 8.** Creamer's Field SNOTEL and AVIRIS-NG summary from 1 April – 1 May.

**Figure 9.** The mean reflectance difference between the field spectrometer and AVIRIS-NG in the visible wavelengths as it relates to the fraction of snow endmember. The fraction of snow endmember was estimated through linear spectral unmixing.

**Figure 10.** The mean reflectance difference between the field spectrometer and AVIRIS-NG in the near-infrared wavelengths as it relates to the fraction of snow endmember. The fraction of snow endmember was estimated through linear spectral unmixing.

**Figure 11.** The mean reflectance difference between the field spectrometer and Landsat 8-9 OLI Surface Reflectance by band as it relates to the fraction of snow endmember. The fraction of snow endmember was estimated through linear spectral unmixing of AVIRIS-NG pixels.

### SUPPLEMENTARY MATERIAL

**Figure S.1.** SNICAR modeled snow surface reflectance using a range of snow grain effective radius values.

**Figure S.2.** Spectral comparison between field spectrometer measurements and modeled SNICAR spectra whose effective grain radius was set to that of the *in situ* measurement.

**Figure S.3.** Spectral comparison between AVIRIS-NG measurements and modeled SNICAR spectra whose effective grain radius was set to that of the *in situ* measurement.

## LIST OF EQUATIONS

**Equation 1.** Generalized equation for albedo, where  $\alpha$  is the albedo,  $S_r$  is solar radiation reflected at the snow surface, and  $S_i$  is the solar irradiance.

**Equation 2.** Linear Spectral Unmixing equation applied to AVIRIS-NG data where  $R_c$  is the surface reflectance of AVIRIS-NG channel  $c$ ,  $F_i$  is the fraction of the endmember  $i$ ,  $R_{i,c}$  is the reflectance of endmember  $i$  in AVIRIS-NG channel  $c$ ,  $n$  is the number of spectral endmembers and  $E_c$  is the residual error.

**Equation 3.** Solar Incident angle (Topographic Correction), where  $i$  is the incident angle,  $s$  is the terrain slope angle,  $z$  is the solar zenith angle,  $a$  is the solar

**Equation 4.** Calculation to apply scale factor and additional offset to Landsat 8-9 OLI bands

**Equation 5.** Application of cosine method, where  $ref_{\lambda}$  is the original band reflectance,  $z$  is the solar zenith angle and  $i$  is the incident angle.

**Equation 6.** Calculation for solar elevation given solar zenith angle.

**Equation 7.** Scaled band area calculation, where  $R_{\lambda}$  is snow reflectance at wavelength  $\lambda$ ,  $R_{\lambda_1, \lambda_2}$  is the continuum reflectance at wavelength defined as the slope between the shoulders of the ice absorption feature, and  $\Delta\lambda$  is the spectral resolution or band w

## 1. INTRODUCTION

### 1.1. Significance

Snow is the brightest substance on Earth, but it is also one of the darkest, depending on the part of the electromagnetic spectrum. In the visible wavelengths, fresh snow has a reflectivity of over 95%, yet in the near-infrared wavelengths, its reflectivity drops to near zero. Snow plays a crucial role in Earth's energy balance due to its high albedo (Wiscombe & Warren, 1980). The albedo of snow, the fraction of solar radiation reflected at the snow surface, is critical not only for the planet's energy balance but also governs the timing and rate of snowmelt on a watershed scale. One-sixth of the world's population relies on seasonal snowpack and glaciers for water resources (Barnett et al., 2005). In the western United States, seasonal snowpack serves as a reservoir to supply growing populations (Hale et al., 2023). Anthropogenic warming is causing an increase in global temperature (Calvin et al., 2023), further leading to changes in precipitation patterns and forest behavior (Musselman et al., 2017; Westerling et al., 2006). Mountain watersheds in the western United States and boreal forests in Alaska are facing two major alterations in a warming climate: decreases in seasonal snowfall and an increase in wildfire activity (Mote et al., 2018; Smith et al., 2021; Westerling et al., 2006). In the seasonal snow zone (Hammond et al., 2018), light absorbing particles (LAPs), such as black carbon and woody debris, are deposited on the snow surface throughout the snowfall season after a wildfire occurs (Gleason et al., 2019; Smoot & Gleason, 2021). The deposition of LAPs decreases the snow surface albedo, increasing the amount of energy absorbed at the snow surface (Gleason et

al., 2013). The combination of LAP deposition and decreased forest canopy cover accelerates snow melt and snowmelt timing (Gersh et al., 2022; Hatchett et al., 2023; Warren & Wiscombe, 1980). Earlier and accelerated snowmelt have significant implications for water resources and management, including vegetation stress and decreases in streamflow (Musselman et al., 2017).

## 1.2. Motivation

A key aspect in which fire affects snow is black carbon and burned woody debris shedding from burned trees, which causes a significant reduction in snow surface albedo (Gleason et al., 2013). Knowledge gaps lie in the levels of uncertainty and variability of snow albedo across varying spatial and temporal scales in snow dominated, forested watersheds. It is especially important to reduce uncertainties in albedo because a relatively small uncertainty in a very bright substance can lead to large errors in estimating the amount of absorbed solar radiation. Letcher & Minder (2015) emphasize the importance, sensitivity, and complexity of the snow albedo parameters in modeling snowpack energy balance. Correctly parameterizing snow albedo, especially across burned landscapes is crucial for seasonal to decadal climate modeling and short-term water forecast accuracy. Moreover, understanding the spatial variability and scaling relationships of snow albedo across heterogeneous landscapes is crucial for supporting future spaceborne missions that will monitor snow properties at global resolution. The spatial resolution and optical instruments of current satellite products makes it challenging to assess snow albedo in forested areas, as optical instruments can't detect material beneath trees. Challenges lie in differentiating land surface albedo from snow albedo. That is, most satellite scenes in snow-

covered forested areas are mixed pixels, with reflectance contributions from vegetation cover, snow, rock, soil, water, and other surface materials that may exist within the instrument's footprint. To bridge the scale of observation gap between ground-based observation and satellite data, new instrumentation, and detailed mixed pixel analysis are necessary.

When comparing existing ground-based, airborne, and satellite observations, the fundamental differences between snow reflectance and albedo must be characterized and quantified so that climate modelers and hydrologists can understand changes in snow and landscape albedo as a function of spatial scale.

### 1.3. Research Objectives

The goal of this research is to characterize snow albedo across different scales of observation in burned forests, unburned forests, and open areas. Ultimately, this work will provide information for future spaceborne missions focused on the role of seasonal snow in hydrology and climate. Our objectives are to:

**Objective 1:** Examine and evaluate spectral snow albedo across different spatial scales and levels of fire disturbance in forested and open areas, and

**Objective 2:** Develop generalizable scaling relationships based on *in situ*, airborne, and spaceborne measurements of snow albedo and reflectance; and

**Objective 3:** Evaluate and compare existing spectral reflectance instrumentation and snow model.

We compare variations of snow surface reflectance in a burned forest, open area, and forested area in the Alaskan Boreal Forest using ground-base, airborne, and satellite

data. We then estimate and compare significant spectral ranges of hyperspectral data from ground-based and airborne spectrometers and a spectral snow model. Comparing snow surface reflectance and albedo observations across spatial scales of observation will enhance our understanding of multiple instruments and model's ability to capture post-fire LAP deposition and spatial variability. It is crucial to untangle the spatial variability of snow albedo as it relates to instrument spatial, spectral and temporal resolution to monitor increasingly vulnerable and changing mountain watersheds within the seasonal snow zone.

## **2. BACKGROUND AND PREVIOUS WORK**

### **2.1. Changing Snow Conditions in a Warming Climate**

As temperature and precipitation patterns change in a warming climate, snowpack is declining (Mote et al., 2018). Most mountain watersheds in the western United States fall within the seasonal snow zone, which is defined as areas with persistent snow throughout the winter season (Hammond et al., 2018). With shallower snowpack due to less winter precipitation and higher seasonal temperatures, snow is melting earlier in these regions (Musselman et al., 2017), resulting in a shortened duration of annual snow-covered days (Mote et al., 2005) and an earlier snow disappearance date (Nolin et al., 2021). Nolin et al. (2021) describe the importance of snow disappearance date as it significantly decreases the landscape albedo, further impacting wildfire activity due to seasonal soil moisture declines (Westerling, 2016). Uncertainties surrounding the timing and quantity of snowmelt are of high importance for water resource management (Stewart et al., 2005).

## 2.2. Wildfire Behavior

Increases in wildfire activity have been attributed to increases in overall temperature and earlier spring snowmelt (Westerling et al., 2006). In addition to anthropogenic climate change, the increase in wildfire activity can also be attributed to fire suppression initiatives and industrialization (Marlon et al., 2012; Parks et al., 2015), which overall increases forest fuel loads and sensitivities (Higuera et al., 2015), in turn decreasing forest resilience. Wildfires have been advancing into the seasonal snow zone at a rate of approximately 7.6 meters per year (Alizadeh et al., 2021). Likely, increases in wildfire activity in the seasonal snow zone (Alizadeh et al., 2021) are associated with, and further accelerating earlier snowmelt. Additionally, the boreal forest region in Alaska is experiencing significant snow declines and fire increases (Randerson et al., 2006).

## 2.3. Snow Albedo

Snow albedo is defined as the ratio of reflected radiation at the snow surface to solar irradiance and is a dominant component of the surface energy budget of snow (Wiscombe & Warren, 1980).

$$\alpha = \frac{S \uparrow}{S \downarrow} \quad \text{Equation 1}$$

Where  $\alpha$  is the albedo,  $S \uparrow$  is solar radiation reflected at the snow surface, and  $S \downarrow$  is the solar irradiance. Shortwave albedo can range from 90 to 50% throughout the accumulation and ablation season (Wiscombe & Warren, 1980). Using satellite-derived data, Robinson & Frei (2000) show that by December, more than 50% of the land above 20° North latitude is snow covered. In a warming climate with less global snow cover, the Earth's surface will absorb more solar radiation and further accelerate melt (Thackeray & Fletcher, 2016).

Snow albedo is influenced by many factors, including temperature, solar angle, snow microstructure, and shading effects (Warren, 1982). With increasing sun angle relative to the snow surface, known as the solar zenith angle, the albedo of dry and melting snow increases (Warren, 1982). The grain size of snow is correlated to the snow albedo. An increase in grain size results in a decrease in snow albedo across all wavelengths. As snow ages, the optical grain size of snow ranges from 50  $\mu\text{m}$  to 1 mm, increasing with snow age (Warren, 1982; Wiscombe & Warren, 1980). Seidel et al. (2016) found that in alpine regions of Colorado and California, snow grain sizes are smaller in colder snowpacks that are found at higher elevations and on north-facing slopes. Thus, in the early ablation period, snow albedo is greater at higher elevations compared to snow albedo values at lower elevations. In addition to snow metamorphism, other factors such as deposition of light-absorbing particles (LAPs) and wind can also affect grain size (Warren & Wiscombe, 1980).

#### **2.4. Snow Grain Size**

Snow grain size influences snow albedo in the near-infrared part of the spectrum (Wiscombe & Warren, 1980). While grain size varies with snow depth, the grain size in the top  $\sim 20$  cm of the snowpack mainly affects albedo. Snow grain size can be measured in the field using a crystal card (Fassnacht et al., 2009). Others have approximated snow grain size by estimating specific surface area (Matzl & Schneebeli, 2006), and others integrate the ice absorption feature to interpolate effective grain radius (Nolin & Dozier, 2000).

#### **2.5. Post-Fire Effects on Snow Albedo Across Spatial Scales**

When a wildfire burns a forested area within the seasonal snow zone (Hatchett et al., 2023), there is a well-documented sequence of events to follow (Gersh et al., 2022;

Gleason et al., 2013, 2019). After a moderate to severe fire, the tree canopy cover decreases (Stevens, 2017). The decrease in canopy cover increases the amount of solar radiation that reaches the snow surface (Gleason et al., 2013). Simultaneously, black carbon (Delaney et al., 2015; Hatchett et al., 2023) and woody debris (Gleason et al., 2013) are deposited on the snow surface, decreasing the snow surface albedo. Pure, undisturbed, fresh snow is estimated to have an albedo in the visible part of the electromagnetic spectrum of about 0.9-0.95 (Wiscombe & Warren, 1980). Snow albedo is much lower in the near-infrared wavelengths, with values depending mostly on snow grain size (Wiscombe & Warren, 1980). Snow albedo decreases as the snow ages due to increasing grain size and accumulation of light absorbing particles (Wiscombe & Warren, 1980; Warren & Wiscombe, 1980; Amaral et al., 2017). This process is referred to as snow albedo decay and is typically expressed as an exponential decay function with an empirically derived coefficient (United States Army Corps of Engineers, 1956). Zolles & Born (2021) have published separate albedo decay functions for dry snow and wet snow. Gleason & Nolin (2016) found that burned woody debris following a forest fire accelerated snow albedo decay. When comparing the spectral albedo throughout the ablation season, they found the greatest variation across visible wavelengths (Gleason & Nolin, 2016). Additionally, during the ablation season, LAPs and forest litter tend to concentrate at the snow surface, further accelerating melt (Gleason & Nolin, 2016). Increased solar irradiance due to decreased canopy cover combined with decreased snow surface albedo due to LAPs, results in accelerated and earlier snowmelt (Gleason & Nolin, 2016). While this phenomenon is well documented at fine spatial scales, it has not yet been fully explored across spatial scales nor incorporated

into snow hydrology and climate models that operate at scales from 100 m to multiple kilometers.

Spatial scale matters because post-fire albedo effects at the landscape scale (~30 m) are opposite of those of the snowpack. Before a wildfire, a forested pixel is dominated by low albedo vegetation, resulting in a low landscape albedo typically ranging from 0.13–0.21 (Betts & Ball, 1997). Snow albedo may be decreased by forest litter (needles, bark dust, cones). Following a wildfire, the dense forest canopy has been removed, exposing the bright snow cover, thereby resulting in a significantly post-fire higher landscape albedo (O'Halloran et al., 2014).

Gersh et al. (2022) found the landscape albedo post-fire to increase by 21%, on average, in the winter following the fire. From a 30-m spatial resolution, the snow-wildfire effect would suggest an increase in albedo, conflicting with the point scale observation of snow albedo decreasing after a wildfire. As previously mentioned, from the point scale, LAPs contaminate the snow, decreasing the snow surface albedo. The variation across spatial scales is summarized in Figure 1. These conflicting observations highlight the complexity between local-scale and broader spatial patterns, requiring a more detailed understanding of the post-fire changes in albedo across scales of observation. Furthermore, we must improve and refine the snow albedo parameterization and snow-wildfire effects in our models to accurately reflect snowmelt patterns in a changing environment (Hao et al., 2022; Hatchett et al., 2023).

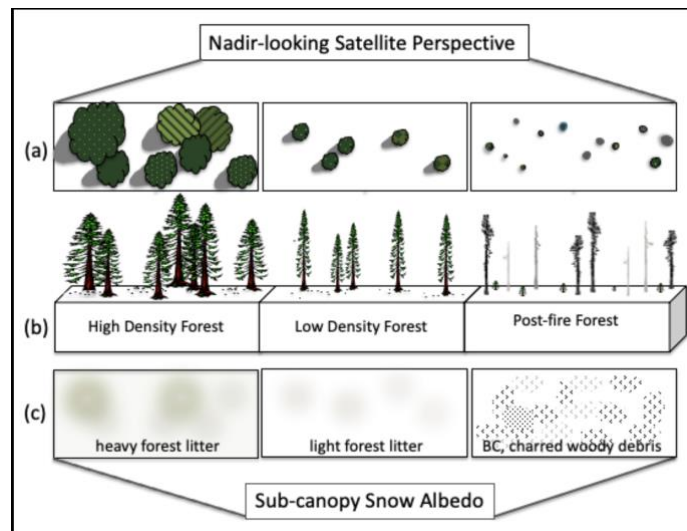


**Figure 1.** The post-fire effect of light absorbing particles (LAPs) on snow covered forested areas across forest densities from varying scales of observation. Section (a) shows the nadir-viewing perspective of forest; (b) shows the side-view; (c) shows the snow surface albedo. Developed by A. Nolin.

## 2.6. Reflectance vs. Albedo

Inconsistencies of terminology in the literature surrounding reflectance and albedo pose challenges when reproducing and comparing scientific results. It has been acknowledged that reflectance terminology is often ambiguous (Schaepman-Strub et al., 2006), and recent studies intermittently specify the correct variable being measured and estimated. Schaepman-Strub et al. (2006) provide a detailed review of reflectance quantities and terminology, particularly dividing the measurable and conceptual quantities into directional, conical, or hemispherical subcategories. Distinguishing between reflectance types depends on the instrument used, and it is crucial to acknowledge when comparing measurements from different sources. For example, when using a right-angle diffuser foreoptic on a field spectrometer to measure incoming and reflected solar energy, the measurement is termed the bi-hemispherical reflectance (Schaepman-Strub et al., 2006).

Alternatively, a reflectance measurement that is made relative to a calibrated reflectance standard is termed “reflectance factor”. Additionally, it is important to acknowledge that the chosen optic may introduce non-snow biases, such as shadows and vegetation. Methods have been developed to convert snow surface reflectance to spectral albedo using radiative transfer models (Seidel et al., 2016).

## **2.7. Snow Albedo and Reflectance Measurement Instrumentation and Models**

### **2.7.1. Field Spectrometer**

Multiple methods have been used to measure snow albedo. The most common approach for collecting ground-based measurements of snow albedo is using a field spectrometer (Nolin & Dozier, 2000). Such instruments acquire data using a fiber optic for incoming light and a diffraction system to split the incoming light into narrow wavelength bands that are incident on a detector. The spectral resolution is typically 1 nm and the spectral range is typically about 380 – 2500 nm. Field spectrometers can measure spectral radiance, irradiance, and reflectance.

Foreoptics are commonly used to constrain the field-of-view (FOV) of the field spectrometer. To measure reflected light within a narrow angle, one uses a foreoptic. Foreoptics can be as narrow as 1° FOV but more often, an 8° FOV foreoptic is used. To measure the full 180° hemisphere, a cosine receptor, also referred to as a right-angle diffuser, is used. This allows the user to measure upward and downward hemispherical radiance, which when ratioed, is the spectral albedo. When collecting measurements of reflectance, an important component of the field spectrometer system is the calibrated

reflectance panel. In this study, we used a 10 cm × 10 cm laboratory calibrated Spectralon™ panel (“Spectralon® Diffuse Reflectance Targets - Durable Reflectance Panels,” n.d.). Since it is not safe for the instrument to point the fiber optic at the Sun, the Spectralon™ panel serves as a proxy for solar irradiance. Measured values of reflected light from the snow are ratioed to values of reflected light from the Spectralon™ panel and the resulting quantity is referred to as the hemispherical-directional reflectance factor (Schaepman-Strub et al., 2006)(Table 1).

### 2.7.2. AVIRIS-NG

In 1983, NASA’s Jet Propulsion Laboratory (JPL) developed the Airborne Visible / Infrared Imaging Spectrometer (Painter et al., 1998). AVIRIS is an airborne imaging spectrometer with a spectral range of 400 to 2500 nm, and 224 contiguous channels with a spectral resolution of 10 nm (*AVIRIS - Airborne Visible / Infrared Imaging Spectrometer - Data*, n.d.) In recent years, NASA JPL began flying the AVIRIS-NG (Next-Generation) instrument. AVIRIS-NG has a spectral range of 280 to 2510 nm, with 481 contiguous channels and a spectral resolution of 5 nm (Chapman et al., 2019). The spatial resolution varies with aircraft altitude. The spatial resolution of the AVIRIS-NG data in this research varies from 4.3 to 4.9 m. Both AVIRIS and AVIRIS-NG measure the hemispherical-conical reflectance factor (Table 1). AVIRIS-NG Imaging spectroscopy is an asset to earth remote sensing as it provides fine-resolution spectroscopy data across large areas. From characterizing wildfire fuel type (Smith et al., 2021) to snow covered terrain (Painter et al., 1998), the instrument is effectively and efficiently used across earth science disciplines.

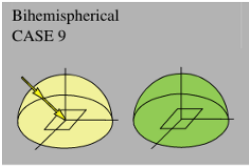
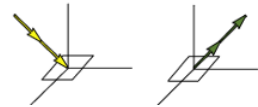
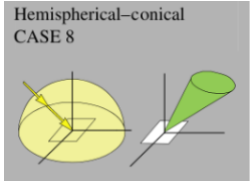
### **2.7.3. Landsat 8-9 OLI Surface Reflectance**

In the last decade, algorithms have been developed to derive snow properties from satellite products (Rittger et al., 2013). Skiles et al. (2023) derive snow albedo from Landsat 9 using the Snow, Ice, and Aerosol Radiative Transfer (SNICAR) model to enhance the effects of light absorbing particle deposition on snow. The Landsat 8-9 Operational Land Imager (OLI) Collection 2 Surface Reflectance product has a spatial resolution of 30 m and a temporal repeat of 8 days (Earth Resources Observation And Science (EROS) Center, 2013). The product accounts for atmospheric correction and is publicly available for download from the United States Geological Survey (USGS) through the Earth Explorer portal. Being a satellite derived product, the reflectance product is characterized as bi-directional reflectance factor (Table 1).

#### **i. Snow, Ice and Aerosol Radiative (SNICAR) model**

The Snow, Ice and Aerosol Radiative (SNICAR) model is used to model spectral albedo of snow across latitudes, throughout seasons and with varying light absorbing particles (LAPs). The SNICAR model is publicly available as a web-based model and allows users to input preferred parameter values. The SNICAR-Adv3 web model produces the modeled spectral snow signature, associated text file (.txt) containing the central wavelength of band (microns), albedo of spectral band, and fraction of incident irradiance within band. Donahue et al. (2021) uses SNICAR to model theoretical snow spectra for a range of effective grain radius, to further calculate scaled band area under various illumination and snow properties. Modeled spectra were then compared to snow samples in a laboratory setting, using near-infrared hyperspectral imaging (NIR-HSI).

**Table 1.** Summary table of measured reflectance quantities discussed in Schaepman-Strub et al. (2006) and applied in this research.

<b>Measured Reflectance Quantities Summary Table</b>			
Type	Bi-Hemispherical Reflectance	Bi-Directional Reflectance Factor	Hemispherical-conical reflectance factor
Definition	The ratio of radiant flux reflected from a unit surface area into the whole hemisphere of the incident radiant flux of hemispherical angular extent	The ratio of reflected radiant flux from the surface area to the reflected radiant flux from an ideal and diffuse surface of the same area under identical view geometry and single-direction illumination	The ratio of the reflected radiance in a conical $8^\circ$ field of view relative to the reflectance from a calibrated Spectralon™ panel
Instrument	Field Spectrometer Cosine Receptor	Landsat 8-9 OLI Surface Reflectance  AVIRIS-NG	Field Spectrometer $8^\circ$ optic and Spectralon™
Illustration	Bihemispherical CASE 9 	Bidirectional CASE 1 	Hemispherical-conical CASE 8 

### 3. RESEARCH METHODS

#### 3.1. Introduction to Snow Albedo Field Campaigns: 2023 and 2024

The research described here is in support of the NASA SnowEx 2023 Snow Albedo Project.

The NASA SnowEx 2023 Snow Albedo Project is supported by NASA's Terrestrial Hydrology

Program (THP) and it contributes to the NASA SnowEx goal of addressing gaps in remote sensing for future snow satellite missions. The objectives of the SnowEx Snow Albedo Project include 1) characterizing snow albedo across spatial scales in burned and unburned forests; 2) evaluating uncertainties in snow albedo in existing remote sensing products, and; 3) developing snow albedo calibration and validation site data for future spaceborne missions.

### **3.1.1. SnowEx Snow Albedo Campaign 2023**

The NASA SnowEx Snow Albedo Campaign in 2023 included a month-long, collaborative field campaign. There were over 20 field participants from multiple institutions and agencies who assisted throughout the campaign. The field campaign occurred in April 2023 in the interior of Alaska outside of Fairbanks. The transects were individually characterized as open, forested, or burned areas. In addition to ground measurements collected with field spectrometers, the campaign also included airborne spectroscopy measurements with NASA JPL's AVIRIS-NG sensor. Ground and airborne measurements were collected when weather conditions permitted, as these measurements require clear sky conditions to minimize changing illumination conditions

### **3.1.2. Terrestrial Hydrology Program - Snow Albedo Campaign 2024**

The goal of the 2024 field season was to fill any missing data gaps that remain from the 2023 field season. These gaps included collecting albedo and reflectance measurements across patchy, melting snow and detailed spectral reflectance measurements of burned and

unburned vegetation, and bare ground. Snow samples were also a major focus of the 2024 campaign; however, those results are not yet analyzed and are not included in this work.

### 3.2. Description of Study Areas

There are three study locations in support of the NASA SnowEx Snow Albedo Campaign: Caribou-Poker Creeks Research Watershed (CPCRW), Creamer's Field, and Delta Junction National Ecological Observation Network (NEON) site (Figure 2). There are seven transects that are characterized as forested, open or burned areas. In 2023, the campaign supported data collection across these transects from 5 April – 5 May. In 2024, data were only collected across burned, forested and open transects in CPCRW on 28 – 29 April.

Of the seven transects measured in 2023, there are 3 open, 2 forested, 1 old burned and 1 recently burned transects. Landscape characteristics for each transect are provided in Table 2.

Due to clear atmospheric conditions and topographic simplicity that facilitated optimal data collection, this research focused on results from the open, old burn at the Delta Junction study site on 20 April 2023. This site and associated measurements are described in more detail in Section 3.9.

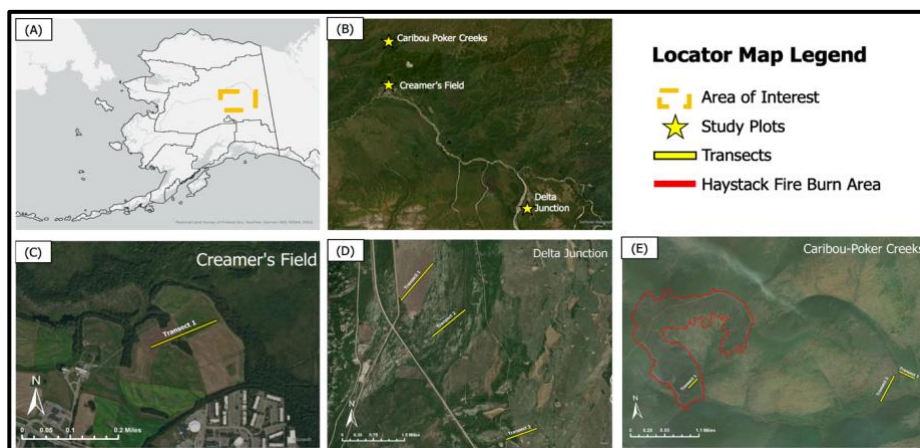


**Figure 2.** Map overview of field study area, where A) general location of campaign in Alaska, B) proximity of sites to one another, C) Creamer's Field site with single transect, D) Delta Junction site with three transects, and E) CPRW site with three ranging transects, including the 2021 Haystack Fire burned area.

**Table 2.** SnowEx Snow Albedo Alaska 2023 campaign transect characterization by location, number, site type (burn, forest, or open), dominant vegetation type, average elevation, topographic setting, and affiliation (Alaska Department of Fish and Game (ASFG), National Ecological Observation Network (NEON), NASA Arctic Boreal Vulnerability Experiment (ABOVE), and/or Long Term Ecological Research (LTER)).

Transect Characterization						
Transect Location	Transect Number	Characterization	Vegetation Type	Average Elevation	Topographic Setting	Affiliation
CPCRW	T1	Burn	Black spruce	370 m	Gentle slope	NEON LTER ABOVE
CPCRW	T2	Forest	Black spruce Birch	248 m	Generally flat	
CPCRW	T3	Open	Shrubland	259 m	Generally flat	
Delta Junction	T1	Open	Shrubland	511 m	Generally flat	NEON
Delta Junction	T2	Forest	Evergreen Black Spruce White Spruce	364 m	Generally flat	
Delta Junction	T3	Open, Old Burn	Shrubland Black Spruce White Spruce	550 m	Generally flat	
Creamer's Field	T1	Open	Shrubland Black Spruce	147 m	Generally flat	ASFG

### 3.3. Field Spectrometer Measurements

#### 3.3.1. Field Sampling

Ground measurements were collected using a Spectral Evolution RS-3500 Portable Spectrometer (SE) and ASD Field Spectrometer (ASD). Both instruments have a spectral range of 350-2500 nm and a spectral resolution of 1 nm. Each transect covered 500-1000

m. This distance was selected to sample spatial variations in forest density, gap size, and forest height. All measurements were collected within two hours of solar noon.

At the start and end of the transect, albedo measurements were acquired using the right-angle diffuser (SE) or cosine receptor (ASD) attachment. These optics measure hemispherical reflectance. The ratio between the upward and downward hemispherical reflectance measurements is the snow surface albedo (bi-hemispherical reflectance, as per Schaepman-Strub et al. (2006)). Each stored value was an average of 10 measurements. Sets of three paired upward- and downward-facing measurements were acquired at the start of each transect. An additional three upward-facing measurements were made to better characterize solar irradiance. Repeat measurements were made to minimize potential bad data or faulty measurements.

Measurements of spectral reflectance factor were made every 10 m along each transect in both the open and burned forests. At each measurement location, we used the 8° foreoptic mounted on the instrument pistol grip, facing directly downward to the snow. Measurements of both snow and calibrated Spectralon™ reflectance panel were made with the operator facing due south. To calculate reflectance factor, and account for variable atmospheric transmissivity, we made multiple, repeat measurements of the Spectralon™ panel beginning at the start of the transect and repeated every 100 m along the transect or every 15 min, whichever came first. Prior to making measurements at each location, the Spectralon™ panel was leveled using a bubble level.

Along the forested transects, the Spectralon™ panel was measured in illumination conditions like those of the adjacent snow surface. For instance, if the snow surface was fully shaded, the Spectralon™ measurement was also made in full shade, likewise for full

sunlit conditions. We attempted to avoid partial shade (“sun dapple”) since it is so highly variable and produces unreliable reflectance values. Rather than collecting measurements every 10 m within a dense forest, 10 measurements were collected in a small arc formation within arm’s reach of the operator. This was meant to capture snow surface albedo variability while maintaining representative lighting conditions.

### **3.3.2. Data Post-Processing**

Field spectrometer data processing and analysis was completed in R Studio (R Core Team, 2023). Spectral Evolution data are in a proprietary file format and were converted to a comma-separated format (csv). In R, the metadata (observation number, latitude, longitude) and data columns (wavelength and reflectance or irradiance), were extracted and compiled into a single csv file for each site. The data and metadata values depend on the data collection settings (e.g., irradiance or reflectance), therefore organized field notes play a crucial role in successful post-processing.

Each spectrum was plotted and assessed to identify data issues. Cold instrument temperature, instrument-tablet communication issues, and human error can negatively impact measurement quality. Noisy data were removed and not used in subsequent calculations. The multiple, co-located Spectralon™ measurements were averaged to create mean reference values against which snow measurements were ratioed. Hemispherical Directional Reflectance Factor (e.g., Schaepman-Strub et al., 2006) was determined by computing the ratio of the 8° reflected radiance measurement over the snow relative to reflected radiance measurement from the Spectralon.

### 3.4. AVIRIS-NG

AVIRIS-NG data from the 2023 NASA SnowEx Snow Albedo campaign are publicly available via the NASA JPL AVIRIS-NG data portal. The products provided by NASA JPL were atmospherically corrected using the algorithm discussed in Thompson et al. (2018). Each flight line available includes a file in band interleaved by line (BIL format) and associated header metadata file (.hdr) in ASCII format.

#### 3.4.1. Visualizing Data in ENVI

AVIRIS-NG reflectance and associated header file were downloaded locally and opened in ENVI to visualize the flight line. Coincident ground-based field spectrometer measurements were mapped onto the corresponding AVIRIS-NG scenes. Each flight was tagged with the closest study site (CPCRW, Delta Junction or Creamer's Field) and corresponding ground transects (T1, T2, T3).

#### 3.4.2. Processing and extracting points of interest using R

The reflectance files were read into R. Due to the orientation of the flight and instrument onboard, some files required rotation using the *rectify* tool in the R package raster. R displays a warning message if the image needs to be rotated and if so, R will prevent any further action until the image is rotated. In this case, it is best to crop the AVIRIS-NG reflectance raster to the bounding box of the transect of interest to reduce processing time. Once the raster was rotated, the shapefile containing ground-based transect spatial coordinates is transformed to the coordinate reference system of the AVIRIS-NG raster. The *extract* tool was then used to extract spectral data from the AVIRIS raster using the spatial coordinate points that make up the ground transect shapefile. For

this study, the spectral data at each coordinate pair, which are the spatial coordinates of the ground observations, were averaged across the transect to compare with *in situ* field spectrometer measurements.

### 3.4.3. Linear Spectral Unmixing

When more than one material is present in the field of view, measurements of snow reflectance from aircraft and satellite result in “mixed pixels”. A mixed pixel is one in which there are multiple components (e.g., vegetation, snow, soil, etc.) each of which contributes to the overall spectral reflectance of the pixel. To understand the effect of multiple land surface components on pixel reflectance requires that we determined the fraction of each component in the pixel. For this, we used linear spectral unmixing (Adams et al., 1986), which uses the spectral reflectance of each component (“endmember”) in a linear model (Equation 2).

$$R_c = \sum_{i=1}^n f_i R_{i,c} + \varepsilon_c \quad \text{Equation 2}$$

where  $R_c$  is the surface reflectance of AVIRIS-NG channel  $c$ ;  $f_i$  is the fraction of the endmember  $i$ ;  $R_{i,c}$  is the reflectance of endmember  $i$  in AVIRIS-NG channel  $c$ ;  $n$  is the number of spectral endmembers; and  $\varepsilon_c$  is the residual error (the difference between the linear modeled reflectance and the measured reflectance in channel  $c$ ). An endmember is a pure spectral representation of a component within a pixel. For example, Figure 3, shows spectral reflectance values for snow and vegetation endmembers as derived from an AVIRIS-NG image acquired on 19 April 2023 from CPRW.

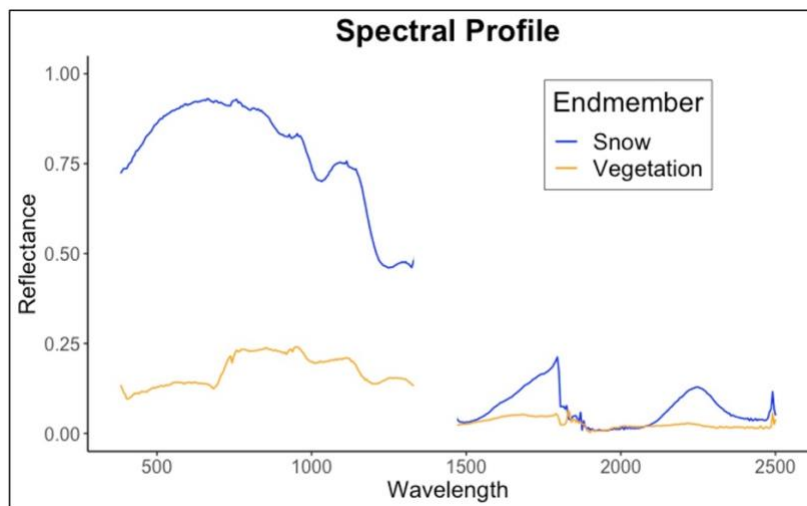


**Figure 3.** Spectral profile of snow and vegetation endmembers selected from within an individual AVIRIS-NG for the linear spectral unmixing analysis.

To understand the effects of mixed pixels on measured reflectance spectra, we made ground-based reflectance measurements of characteristic snow, vegetation, and bare ground. The Spectralon™ was used as the white reference for the endmember measurement in order to capture appropriate lighting conditions. Five to ten reflectance measurements were taken of each endmember. The mean of the reflectance values was then divided by the Spectralon™ measurements across all spectral bands. Additionally, photos of each target were taken for reference and to pair with the endmember spectral signatures.

Linear Spectral Unmixing was completed in the image processing software, ENVI®. The analysis was performed on all AVIRIS-NG scenes that had coincident ground field spectrometer measurements. Endmembers were selected from within each AVIRIS-NG scene to reduce uncertainty from differing atmospheric conditions and instrument or flight orientation. From each scene, a snow and vegetation endmember were selected from pixels surrounding the transect. We subjectively selected the endmembers from areas that appear

to be homogeneous. AVIRIS-NG channels 190–199, or wavelengths 1328–1373 nm, were removed to exclude noisy data that caused by low instrument signal-to-noise. Once appropriate end members were selected, we constrained the sum of the endmember fractions to 1. After running the Linear Spectral Unmixing mapping tool in ENVI with the endmembers selected, the software outputs a raster file with layers corresponding to each endmember and an associated root-mean-square deviation (RMSE) layer. The raster files were then read into R, and transect shapefiles were used to extract points of interest. The extraction process is described in the previous section.

### 3.5. Geolocation Accuracy

The Spectral Evolution RS-3500 is paired via Bluetooth to an Algiz 8X rugged handheld tablet. The tablet utilizes a u-blox module which is supported by GPS and GLONASS, allowing the tablet to provide GPS coordinates for each saved measurement. During the 2023 campaign, transect measurements taken with all other field spectrometers were spatially referenced using a Mesa Rugged Tablet. Airborne data from AVIRIS-NG were geolocated with an INS/GPS system (Bhattacharya et al., 2019).

### 3.6. Landsat 8-9 OLI

The Landsat 8-9 OLI Surface Reflectance products were downloaded from the U.S. Geological Survey (USGS) EarthExplorer portal (U.S. Geological Survey, 2012) and visualized in ENVI. Landsat scenes were co-located and concurrent with the ground field spectrometer measurements. There were three cloud-free, Landsat 8-9 OLI scenes with coincident *in situ* field spectrometer measurements taken within 24 hours of the satellite overpass. The Landsat scenes and *in situ* measurements covered open, forested and burned

areas. The Landsat 8-9 OLI Surface Reflectance Level 2 product is atmospherically corrected. To account for varying topography, the imagery was topographically corrected using the cosine method outlined in Traversa et al. (2021). The first step in applying the cosine method is an illumination model which is represented by Equation 3 and represents the cosine of the solar incident angle based on a digital elevation model (DEM).

$$\cos(i) = \cos(s)\cos(z) + \sin(s)\sin(z)\cos(a - o) \quad \text{Equation 3}$$

where  $i$  is the incident angle,  $s$  is the terrain slope angle,  $z$  is the solar zenith angle,  $a$  is the solar azimuth angle and  $o$  is the terrain aspect angle. The solar azimuth and solar zenith angle were extracted from the Landsat scene metadata. The terrain slope angle and aspect angle were estimated using the USGS 5m Digital Elevation Model (DEM) product. The DEM was reprojected to 30-m spatial resolution to align with the Landsat product. It is important to note that the scale factor and additional offset were applied to each band prior to topographic correction (Equation 4).

$$\text{band}_{\text{corrected}} = (\text{band} * 0.0000275) - 0.2 \quad \text{Equation 4}$$

The cosine method applies the calculated incident angle in the following formula:

$$\text{ref}_c = \frac{\text{ref}_o * \cos(z)}{\cos(i)} \quad \text{Equation 5}$$

where  $\text{ref}_o$  is the original band reflectance,  $z$  is the solar zenith angle and  $i$  is the incident angle. Using the topographically corrected Landsat data, pixels were selected based on coordinates associated with coincident transects. The Landsat surface reflectance values were averaged across each transect for each band (Table S.1). Coincident field spectrometer data were aggregated to the spectral range of Landsat bands (Table 3).

**Table 3.** *Spectral band description and wavelength range of Landsat 8-9 Operational Land Imager (OLI) Collection Surface Reflectance data.*

Landsat 8-9 OLI Spectral Band Ranges	
Band	Spectral Range
Band 1 - Visible Coastal Aerosol	0.43 – 0.45 $\mu\text{m}$
Band 2 - Visible Blue	0.45 – 0.51 $\mu\text{m}$
Band 3 - Visible Green	0.53 – 0.59 $\mu\text{m}$
Band 4 - Red	0.64 – 0.67 $\mu\text{m}$
Band 5 - Near-Infrared	0.85 – 0.88 $\mu\text{m}$
Band 6 - SWIR 1	1.57 – 1.65 $\mu\text{m}$
Band 7 - SWIR 2	2.11 – 2.29 $\mu\text{m}$

### 3.7. Statistical Analyses

#### 3.7.1. Reflectance Comparisons

A series of statistical tests were performed to compare reflectance values from field spectrometers and AVIRIS-NG. AVIRIS-NG and field spectrometer reflectance values were subset into three spectral regions: visible (400-700 nm, VIS), Near-Infrared (700-950, NIR), and Ice Absorption Feature (950-1090 nm) (Table 4).

**Table 4.** *Spectral regions with associated spectral range (1 nm) and AVIRIS-NG channels (5 nm intervals)*

Spectral Region	Spectral Range (1 nm)	AVIRIS-NG Spectral Range (5-nm intervals)
Visible	400–750 nm	402–747 nm
Near Infrared	780–900 nm	782–898 nm
Ice Absorption Feature	950–1090 nm	953–1088 nm

The data were also subset by site type: open, burn, or forest. First, we ran a Levene test to assess if variances of sample populations for all instruments and site types are equal.

The results of the Levene test determine which type of ANOVA would be run (e.g., Welch ANOVA). To further break this down by spectral region, we applied a Games Howell Test to compare the means for each spectral subset (VIS, NIR, Absorption Feature), for each site type. The Games Howell Test accounts for unequal variances between groups (*Games Howell Post-Hoc Tests — Games\_howell\_test*, n.d.). We did not run these tests to compare Landsat 8-9 and field spectrometer reflectance due to an insufficient sample size.

### 3.7.2. Scaling Relationships

We aim to understand how reflectance changes as a function of spatial scale. To do this, we compared mean reflectance differences between coincident field spectrometer, AVIRIS-NG, and Landsat 8-9 data as a function of the fraction of the snow endmember in each pixel. We used the AVIRIS-NG-derived snow cover fraction for both the AVIRIS-NG and Landsat data. The functional forms of these two scaling relationships were determined statistically and graphically.

### 3.8. Estimating Effective Grain Radius with SNICAR

To use SNICAR to estimate the spectral signature of pure snow with a grain size equivalent to that of *in situ* ground measurement, a lookup table was created using approximate input parameters of the *in situ* conditions. NOAA's Solar Position Calculator was used to estimate the solar elevation, which was then used to calculate the solar zenith angle across all days where ground measurements were taken.

$$\text{solar elevation} = 90^\circ - \text{SZA}$$

*Equation 6*

where solar elevation is the output from the National Oceanic and Atmospheric Administration's (NOAA) solar position calculator, and SZA is the solar zenith angle. All ground measurements for the NASA SnowEx campaign were collected within two hours of solar noon. For computational purposes, we calculated the average solar zenith angle within two hours of solar noon for each date and location using the center point of each transect. The solar zenith angles are listed in Table S.2. The average solar zenith angle ( $55.2^\circ$ ) was then used for the solar zenith parameter in SNICAR. The incident radiation options are direct or diffuse. Due to clear-sky atmospheric conditions, direct was chosen for all simulations (Flanner et al., 2021). Due to the campaign's location and season, Sub-Arctic Winter was chosen for the surface spectral irradiance conditions. The average snowpack thickness and densities were estimated to 1 m and  $20 \text{ kg/m}^3$  respectively. Ice refractive index data input were set to the "Picard et al. (2016)/ Warren & Brandt (2008)" option. The snow grain shape parameter was set to spheroids, with a default aspect ratio of 0.5. The broadband albedo of the underlying ground remained at the model default of 0.25. The model was run with snow grain effective radii ranging from 30-1500  $\mu\text{m}$ , which are the set minimum and maximum, respectively, for the online version of SNICAR. All concentration parameters were set to zero. The purpose of comparing the SNICAR modeled spectra to *in situ* ground measurements is to compare how SNICAR models 'pure snow' under the predetermined conditions. The snow surface is likely contaminated with black carbon, woody debris and vegetation shadows, as well as the field of view being affected by human-error such as participant shadows and bodies. All parameter decisions are summarized in Table 5.

**Table 5.** Parameters and corresponding values selected for SNICAR-Adv3: Online Snow Albedo Simulator.

SNICAR-ADv3: Online Snow Albedo Simulator Parameters	
Model Feature	Parameter Selection
Incident radiation	Direct
Solar zenith angle (SZA)	55°
Surface spectral irradiance conditions	Sub-Arctic Winter
Snowpack thickness	1 m
Snowpack density	200 kg/m <sup>3</sup>
Ice refractive index data	Picard et al. (2016) /Warren & Brandt (2008)
Snow grain shape	Spheres
Broadband albedo of underlying ground	0.25
Snow Grain Effective Radius	30 – 1500 μm

The SNICAR-Adv3: Online Snow Albedo Simulator produces an output file with wavelength and reflectance with a spectral resolution of 10 nm. Each output spectrum was tagged with the effective grain size input (Figure S.1). There are a total 12 bands within the spectral range of 975 to 1085 nm. Scaled band area was then calculated from the simulated spectra by integrating over the continuum-scaled ice absorption feature as discussed in detail in (Nolin & Dozier, 2000).

$$\text{Scaled Band Area} = \int_{\lambda=975 \text{ nm}}^{\lambda=1085 \text{ nm}} \frac{R_{\text{cont},\lambda} - R_{\text{snow},\lambda}}{R_{\text{cont},\lambda}} d\lambda \quad \text{Equation 7}$$

where  $R_{\text{snow},\lambda}$  is snow reflectance at wavelength  $\lambda$ ,  $R_{\text{cont},\lambda}$  is the continuum reflectance at wavelength defined as the slope between the shoulders of the ice absorption feature, and  $\Delta\lambda$  is the spectral resolution or band width. The continuum line is shown as a dashed red line in Figure 4.

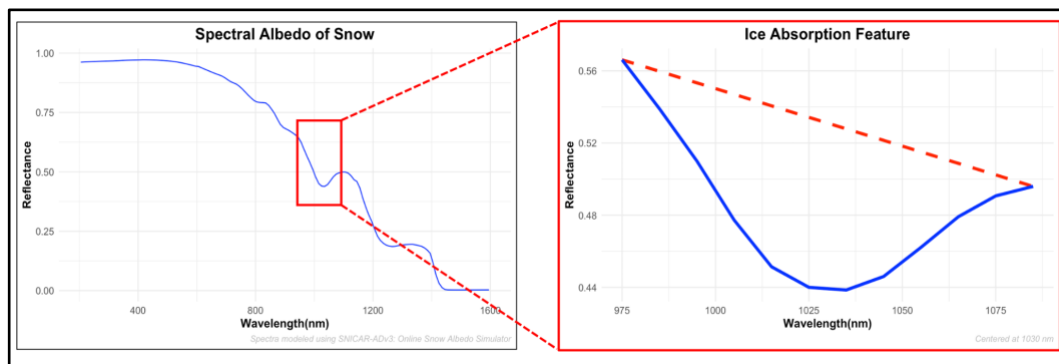


**Figure 4.** Scaled band area method to estimate effective grain radius, where the dashed red line is the continuum and solid blue line is reflectance. Spectra represents SNICAR output of an effective grain radius of 850  $\mu\text{m}$ .

The scaled band area generated from the SNICAR modeled spectral signature is then stored with the respective effective grain size radius in a look up table (Table S.3). In addition to the spectral output, the SNICAR-ADv3: Online Snow Albedo Simulator produced values of broadband snow albedo, which are shown in Figure 5.

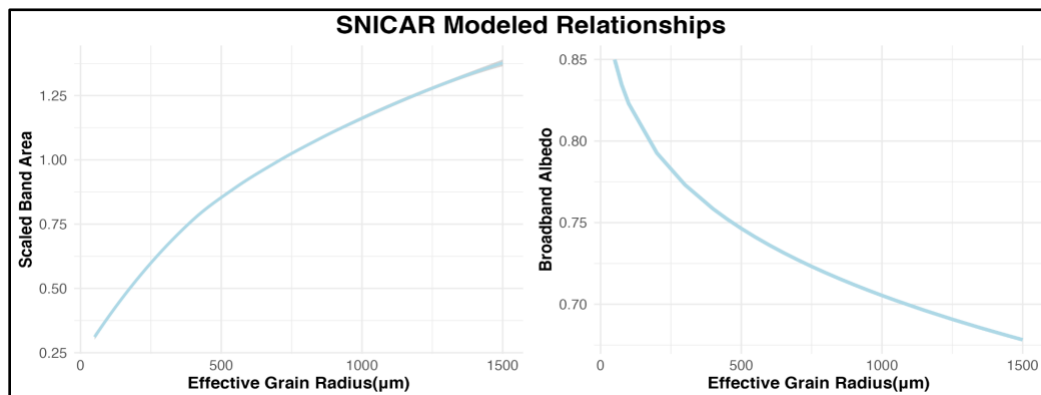


**Figure 5.** Modeled relationship between calculated scaled band area and effect grain radius (left) and relationship between broadband albedo and effective grain radius (right). Data produced using the SNICAR-ADv3: Online Snow Albedo Simulator.

### 3.8.1. Calculating Scaled Band Area and Effective Grain Radius for Ground-based and Airborne Measurements

Since the SNICAR modeled relationship between SBA and effective grain radius will be used to interpolate effective grain radius for *in situ* field spectrometer measurements and airborne AVIRIS-NG data, all hyperspectral reflectance data must be scaled to spectral resolution of SNICAR (10nm). The resampling approximation was completed using the rolling average function in R, *rollapply*. The rolling average for bands aligning with SNICAR output bands were used for the SBA calculation (Equation 6). The lookup table (Table S.3) and modeled relationship (Figure 5) were then used to interpolate effective grain radius using the calculated ground-based and airborne measurements' SBA values (Table 6 and Table 7).

**Table 6.** Calculated scaled band area and estimated snow grain radius for average snow reflectance from field spectrometer measurements. Transects were chosen if they have coincident airborne measurements. Spectra of field spectrometer and SNICAR modeled spectra are provided in Figure S.2.

Field Spectrometer SBA and Effective Grain Radius Coincident with AVIRIS-NG Flights			
Location and Transect	Date	Scaled Band Area	Effective Snow Grain Radius
CPCRW, T1	04/07/2023	0.52	176
CPCRW, T2	04/07/2023	0.56	200
Delta Junction T2	04/13/2023	0.53	179
Delta Junction, T1	04/13/2023	0.46	137
CPCRW, T1	04/14/2023	0.59	229
Creamer's Field, T1	04/15/2023	0.66	283
CPCRW, T1	04/19/2023	0.72	347
CPCRW, T2	04/19/2023	1.02	751
CPCRW, T3	04/19/2023	0.72	351
Delta Junction, T1	04/20/2023	0.66	283
Delta Junction, T2	04/20/2023	0.76	387
Delta Junction, T3	04/20/2023	0.71	341

SNICAR was then run using the interpolated effective grain radius, rounded to the nearest whole number to remove faults precision. The spectral output from SNICAR allowed comparison to the *in situ* spectral measurements to SNICAR modeled, 'pure snow' measurements. Next, we ran SNICAR with the interpolated effective grain radius values from the ground and airborne measurements (Table 6 & Table 7). All SNICAR outputs were

then plotted with the paired *in situ* measurements. Graphs comparing spectra are shown in Figure S.2 and Figure S.3.

**Table 7.** Calculated scaled band area and estimated snow grain radius for average snow reflectance from AVIRIS-NG data. Transects were chosen if they have coincident ground measurements. Spectra of AVIRIS-NG and SNICAR modeled spectra are provided in Figure S.3.

AVIRIS-NG SBA and Effective Grain Radius <i>Coincident with In-Situ Field Spectrometer Measurements</i>			
Location and Transect	Date	Scaled Band Area	Effective Snow Grain Radius
CPCRW, T1	04/07/2023	0.59	228
CPCRW, T2	04/07/2023	0.51	167
Delta Junction T2	04/13/2023	0.62	249
Delta Junction, T1	04/13/2023	0.66	289
CPCRW, T1	04/14/2023	0.57	212
Creamer's Field, T1	04/15/2023	0.57	208
CPCRW, T1	04/19/2023	0.72	346
CPCRW, T2	04/19/2023	0.74	366
CPCRW, T3	04/19/2023	0.67	300
Delta Junction, T1	04/20/2023	0.54	189
Delta Junction, T2	04/20/2023	0.85	495
Delta Junction, T3	04/20/2023	0.62	256

### 3.9. Open, Old Burn Characterization

To assess the instruments' ability to quantify snow surface reflectance across different spectral regions, we focused on a transect characterized as an open, old burn. There are the least number of mixed pixels across the open transect selected compared to other transects. Additionally, there are 28, well-spaced *in situ* measurements taken with the field spectrometer on the chosen day across the chosen transect. The transect in Delta Junction,

Alaska is also relatively flat. On 20 April 2023, atmospheric conditions were optimal for AVIRIS-NG and field spectrometer measurements. The average reflectance across wavelengths within the visible and near-Infrared portions of the spectrum were calculated for each individual point locations for AVIRIS-NG and the Field Spectrometer. To calculate the effective grain radius for AVIRIS-NG data, the bands were interpolated to a 1 nm spectral resolution to calculate scaled band area. Using the SNICAR modeled relationship between scaled band area and effective grain radius, AVIRIS-NG scaled band area values were interpolated to effective grain radius.

#### **4. RESULTS**

Instrument comparisons show that reflectance measurements from airborne and satellite sensors have their greatest agreement with ground-based reflectance measurements in open areas, compared to burned and unburned forested areas. Differences between AVIRIS-NG and field spectrometer measurements, when compared by spectral region, are lowest in open areas (mean difference = 0.09) and highest in forested areas (mean difference = 0.42). These differences are predominantly due to mixed pixel effects, which result when both vegetation and snow are present in the ground-instantaneous field of view of airborne and spaceborne sensors. Here, we present our results from linear spectral unmixing to understand the mixed pixel effect and characterize the transect in terms of fractions of vegetation and snow in AVIRIS-NG and Landsat pixels. We also present a comparison of effective snow grain radius between AVIRIS-NG and field spectrometer, derived using the SNICAR model as previously described.

## 4.1. Statistical Analyses

### 4.1.1. Reflectance Comparisons

We ran a series of statistical tests to compare the reflectance values from field spectrometers and AVIRIS-NG. The Levene test returned a p-value of  $<2.2e-16$ , indicating significantly different variances between all instruments and site types. Due to the significant p-value of the Levene test, we then ran a Welch ANOVA, and this test returned a p-value of zero, indicating that the means are statistically different. The Games Howell test returned a p-value of less than 0.001 for all pairs of groups, indicating that the means across different site types are statistically different for the spectral regions. The results of the Games Howell Test are described in Table 8. One of the outputs from the Games Howell Test is the difference between means, computed as mean field spectrometer reflectance minus the mean AVIRIS-NG reflectance for each spectral region and site type (Figure 6). The relationships are further visualized in Figure 6 as box and whisker plots, where there is the greatest difference in median in the forested area across all spectral ranges and the smallest difference in median in the open area across all spectral ranges. By default, box and whisker plots use the median rather than the mean thus, we show the difference in median values in Table 9.

**Table 8.** Results for Games Howell statistical test, comparing instruments (AVIRIS-NG and field spectrometer) across spectral subsets and site types. All comparisons show statistically significant differences.

Games Howell Test Output				
Relationship by instrument & spectral region	Mean Difference	Confidence Interval Low	Confidence Interval High	p-value
Open-VIS	0.19	0.18	0.20	<.001
Open-NIR	0.06	0.05	0.07	<.001
Open-Absorption Feature	0.03	0.01	0.04	<.001
Forest-VIS	0.57	0.55	0.58	<.001
Forest-NIR	0.40	0.38	0.42	<.001
Forest-Absorption Feature	0.29	0.27	0.32	<.001
Burn-VIS	0.33	0.32	0.34	<.001
Burn-NIR	0.17	0.16	0.18	<.001
Burn-Absorption Feature	0.09	0.07	0.10	<.001

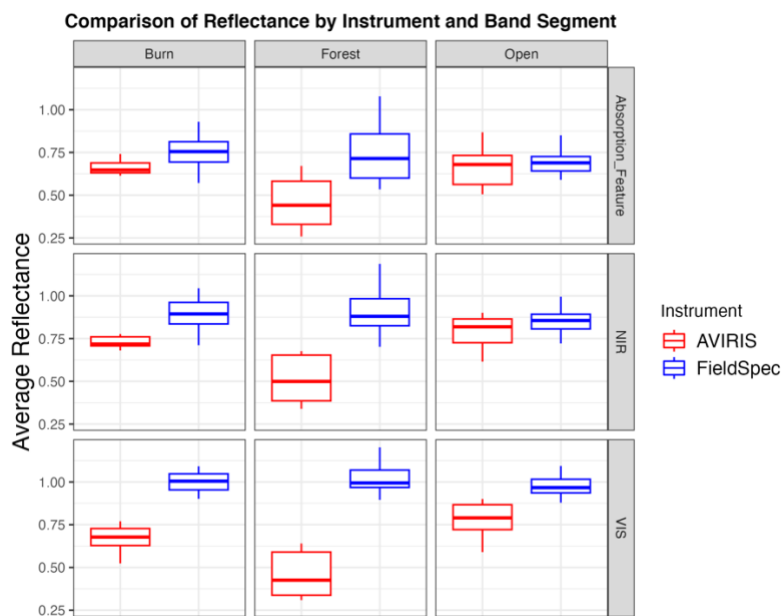


**Figure 6.** Box and Whisker plots comparing average reflectance between instruments grouped by site type and spectral region.

**Table 9.** *The difference in median of AVIRIS-NG and the field spectrometer grouped by spectral region and site type. Data visualized in Figure 6.*

<b>Difference in Median Reflectance</b>			
<b>Spectral Region</b>	<b>Burn</b>	<b>Forest</b>	<b>Open</b>
Absorption Feature	0.11	0.27	0.01
Visible	0.33	0.57	0.18
Near Infrared	0.18	0.38	0.04

We compared reflectance and estimated effective grain size at the open, old burn transect in Delta Junction (described in Section 3.9). The results of this analysis are summarized in Figure 7 and Table 10. We found the field spectrometer median reflectance in the visible wavelengths (0.94) were 13.64% greater than the AVIRIS-NG median reflectance (0.82). There was no difference between the field spectrometer (0.80) and AVIRIS-NG (0.80) reflectance medians in the near-infrared wavelength. The median effective grain radius of the field spectrometer (305  $\mu\text{m}$ ) was 3.67% greater than the median effective grain radius of AVIRIS-NG (294  $\mu\text{m}$ ).

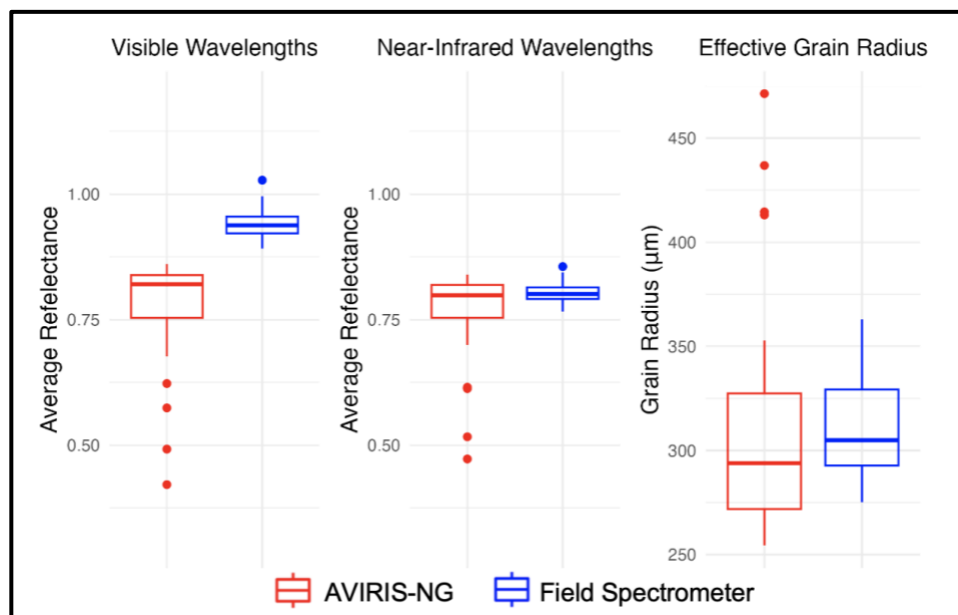


**Figure 7.** Box and Whisker plots comparing average reflectance in the visible and near-infrared wavelengths by instrument across a transect characterized as open. Effective Grain Radius estimated using SNICAR modeled relationship.

**Table 10.** Summary statistics associated with box and whisker plots (Figure 7). Comparison of individual open (historic burn) transect broken down by instrument and spectral region. The instruments include a field spectrometer (FS) and AVIRIS-NG (AV).

Box and Whisker Summary Statistics				
Spectral Region	AV (Median)	FS (Median)	AV (Range)	FS (Range)
Visible	0.82	0.94	0.421–0.86	0.89–1.028
Near-Infrared	0.80	0.80	0.47–0.84	0.77–0.86
Effective Grain Radius	294	305	254–471	275–363

#### 4.1.2. Scaling Relationships

Results of the reflectance differences between field spectrometers, AVIRIS-NG and Landsat 8-9 versus the fraction of snow cover in a mixed pixel are shown in Figures 9-11. We compared the reflectance difference and snow fraction in the visible wavelengths and

near-infrared wavelengths. These figures show a negative relationship between reflectance difference and snow fraction. As the fraction of snow cover increases, the mean reflectance difference between the field spectrometer and AVIRIS-NG decreases (Figures 9-10). All linear regressions have a negative slope, signifying that as the fraction of snow cover increases, the mean reflectance differences decrease. These results further support the previous suggestion that the agreement between instruments is dependent on mixed pixels caused by varying transect composition.

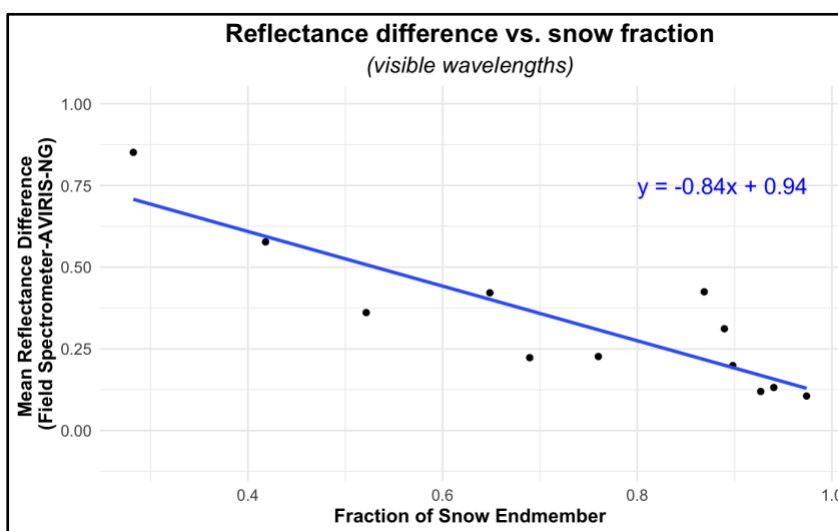


**Figure 9.** The mean reflectance difference between the field spectrometer and AVIRIS-NG in the visible wavelengths as it relates to the fraction of snow endmember. The fraction of snow endmember was estimated through linear spectral unmixing.

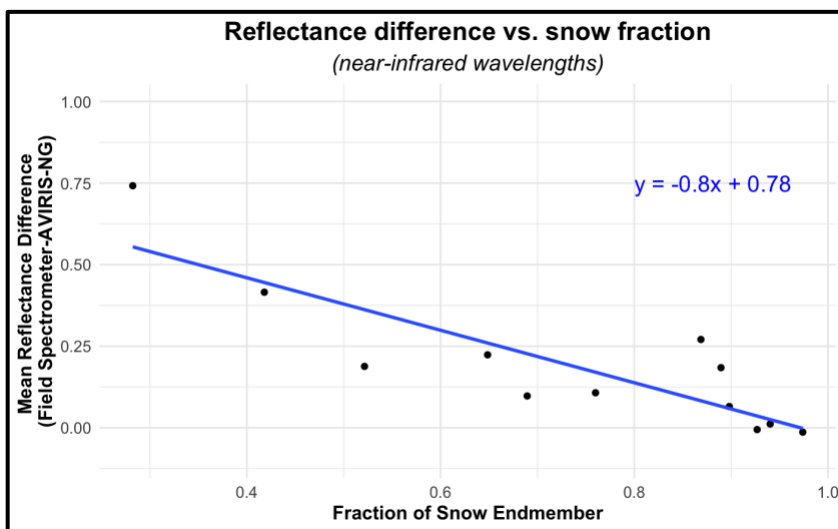


**Figure 10.** The mean reflectance differences between the field spectrometer and AVIRIS-NG in the near-infrared wavelengths related to the fraction of snow endmember. The fraction of snow endmember was estimated through linear spectral unmixing.

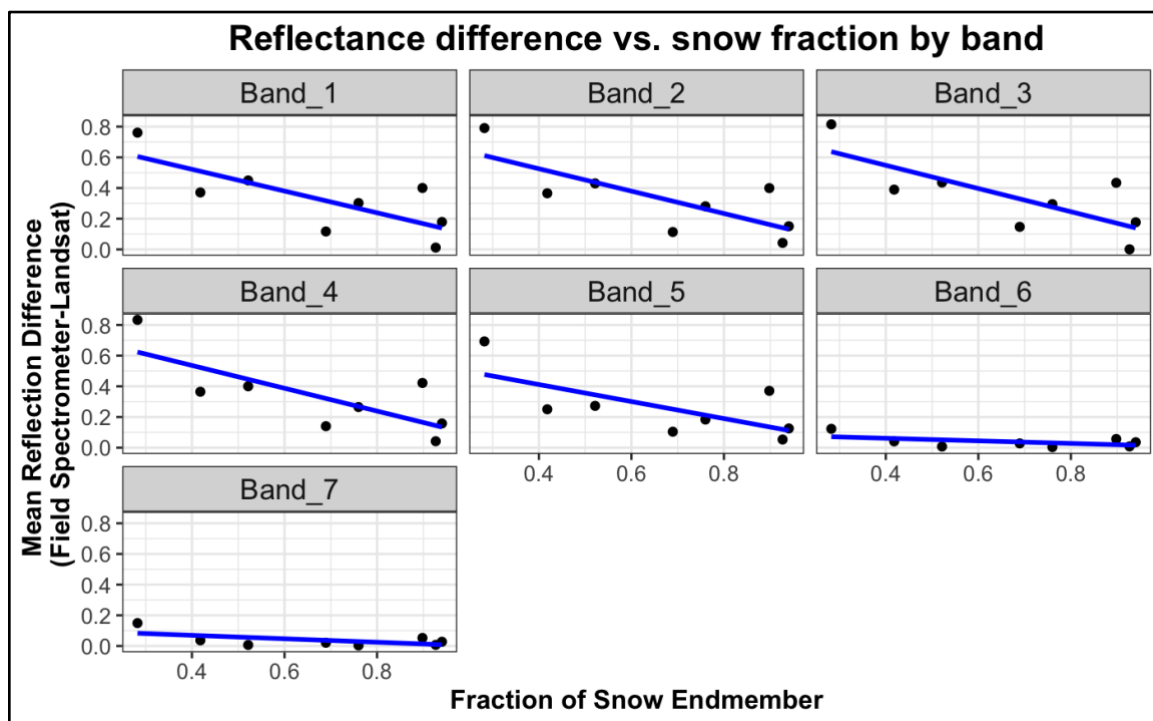


**Figure 11.** The mean reflectance differences between the field spectrometer and Landsat 8-9 OLI Surface Reflectance by band relates to the fraction of snow endmember. The fraction of snow endmember was estimated through linear spectral unmixing of AVIRIS-NG pixels.

The difference was computed as the mean field spectrometer reflectance minus the mean Landsat band reflectance (Table S.1). After grouping by site type, we found there is most agreement between the field spectrometer and Landsat 8-9 in open areas, and least agreement in forested areas (Table 11).

**Table 11.** *The average difference between Landsat 8-9 OLI and coincident field spectrometer (aggregated to Landsat 8-9 OLI spectral range) by site type.*

<b>Reflectance Average of Differences</b>			
Characterization and Band			
<b>BAND</b>	<b>OPEN</b>	<b>FOREST</b>	<b>BURN</b>
Band 1	0.18	0.53	0.30
Band 2	0.18	0.53	0.28
Band 3	0.19	0.55	0.30
Band 4	0.19	0.53	0.27
Band 5	0.16	0.41	0.18
Band 6	0.03	0.06	0.00
Band 7	0.03	0.06	0.00
Overall Average	0.14	0.38	0.19

#### 4.2. AVIRIS-NG Scaled Band Area and SNOTEL relationship

The month of April is typically the ablation season. The weather during the 2023 campaign (1 April – 5 May) was unseasonably cold. To demonstrate the general relationship between weather and snow conditions throughout the 2023 campaign, we compare SNOTEL data to AVIRIS-NG flights over Creamer's Field. The Creamers Field site was chosen for this comparison because 1) there is a SNOTEL station in proximity to the ground

transect, 2) there were 8 cloud-free AVIRIS-NG flights over this site throughout the campaign and 3) the transect is characterized as open, thus has a small fraction of non-snow endmembers when snow covered. The top plot in Figure 8 summarizes the average daily air temperature (Fahrenheit) and average daily snow depth (inches). The bottom two plots show the temporal variation of scaled band area and interpolated effective grain radius, which were calculated based on AVIRIS-NG data over the Creamer's Field transect. The data were constrained to 1 April – 1 May because they were the first and last day of cloud-free, AVIRIS-NG flights, respectively.

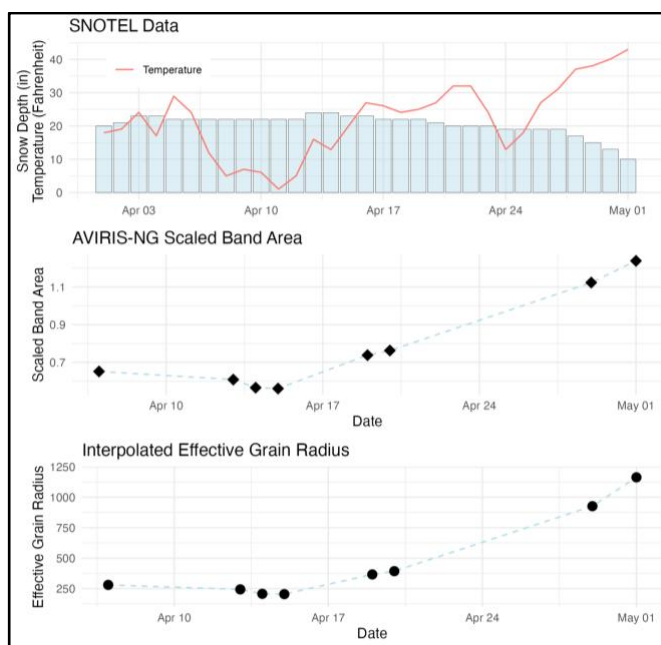


**Figure 8.** Creamer's Field SNOTEL and AVIRIS-NG summary from 1 April – 1 May.

#### 4.3. Linear Spectral Unmixing

Linear spectral unmixing was run on AVIRIS-NG scenes with coincident ground measurements. The geometric mean of each endmember was calculated and normalized to ensure the fraction of each endmember sums to 1. The results were then grouped and summarized by transect (Table 12).

**Table 12.** Results from Linear Spectral Unmixing analysis on AVIRIS-NG scenes with coincident ground observations. The table is grouped by transect characterization (Burn, Forest, Open). The data presented are the normalized geometric mean of pixels containing snow or vegetation. The RMS error (RMSE) describes how representative the end members are of the AVIRIS-NG pixels.

Linear Spectral Unmixing Results			
Burned Transect	Snow	Burn Vegetation	RMSE
CPCRW, 04/07	0.91	0.09	0.007
CPCRW, 04/14	0.90	0.10	0.005
Forest Transect	Snow	Vegetation	RMSE
CPCRW, 04/07	0.76	0.24	0.010
CPCRW, 04/19	0.71	0.29	0.019
Delta Junction, 04/13	0.32	0.68	0.015
Open Transect	Snow	Vegetation	RMSE
CPCRW, 04/19	0.93	0.07	0.010
Creamer's Field, 04/15	0.96	0.04	0.009
Delta Junction, 04/13	0.98	0.03	0.007
Delta Junction, 04/20	0.96	0.04	0.009
Delta Junction (Old Burn), 04/20	0.80	0.20	0.015

#### 4.4. Spectral Library

The spectral library was created to improve characterization of the Alaskan boreal forest during ablation season. Notably, spectral endmembers vary depending on lighting conditions. This difference should be acknowledged in future spectral unmixing efforts. The product includes averaged spectral measurements and photos as reference (Appendix, Spectral Library).

## 5. DISCUSSION

### 5.1. Overview of Key Findings

#### 5.1.1. Linear Scaling Relationships

The most important finding from this study is that there is a linear relationship between reflectance differences at different spatial scales and the fraction of snow cover in a mixed pixel. Using the fraction of snow cover in a mixed pixel as derived from AVIRIS-NG spectral unmixing, we plotted the difference in reflectance (ground-based reflectance minus airborne or satellite reflectance) vs. snow cover fraction in a mixed pixel. We found in all cases that as the snow cover fraction increases, the reflectance differences decrease. This means that if we know the snow fraction in a pixel, and we have measured the reflectance at one scale, then we can linearly interpolate to estimate the reflectance that would be measured at a finer or coarser scale. Moreover, if we can assume that albedo generally tracks with reflectance, we can estimate landscape albedo at different spatial scales.

Further, for pixels that are entirely snow covered, the linear relationship can be simply related to the fraction of vegetation cover in a pixel. If the vegetation percentage is already known (perhaps determined *a priori* from independent satellite measurements), and we know that the snow cover is continuous across the ground area, we can then interpolate what the reflectance is as a function of vegetation fraction. If the snow cover is not continuous, we first would need to estimate snow cover fraction from spectral unmixing, requiring multispectral or hyperspectral data, thereby adding an extra step.

In general, we expect measurements across spatial scales to closely agree in open areas relative to forested areas. We expect to see the least agreement between the airborne

or satellite reflectance when compared to ground reflectance measurements in forested areas because of the presence of non-snow components (e.g., forest canopy, bare ground) within in the field of view at the airborne and satellite scales.

### **5.1.2. Reflectance Comparison by Instrument, Spectral Regions, and Site Type**

All relationships assessed in the Games Howell Test have a p-value less than 0.001, suggesting that there is a significant difference between reflectance measurements from the field spectrometer and AVIRIS-NG. All mean difference values were positive, which suggests the field spectrometer measures reflectance on average higher than AVIRIS-NG. Assessing by site type, we see the greatest overall differences of reflectance in forested areas (mean difference = 0.42) and least overall differences in the open sites (mean difference = 0.09). Conceptually this means that there is most disagreement between AVIRIS-NG and the field spectrometer at the forested sites, and most relative agreement between the instruments at the open site compared to the forested and burned sites.

Similarly, there is the greatest difference between the Landsat 8-9 OLI Surface Reflectance product and the field spectrometer in the forested areas (mean difference = 0.38), compared to the open (mean difference = 0.14) and burned areas (mean difference = 0.19). The difference between instrument reflectance values is due to differences in spatial resolution. The AVIRIS-NG and Landsat data over the burned and forested sites contain mixed pixels, that is a portion of each pixel contains non-snow endmembers, such as trees and other vegetation. We would expect to see the most agreement between instruments in

the sites characterized as open, where there are less mixed pixels and greater snow-only pixels.

### **5.1.3. Comparison of Effective Grain Radii Across Scales**

The difference between the medians of effective grain radius is 11  $\mu\text{m}$  is small relative to overall snow grain size which ranges from 254–471  $\mu\text{m}$ . The agreement between ground based and AVIRIS-NG grain size retrievals suggests that we can accurately estimate grain size over relatively large areas using airborne hyperspectral instruments. Remotely sensed grain size estimates are far more efficient than field-based methods of grain size retrievals using such instruments as IceCube (Zuanon, 2013).

### **5.1.4. Creamer’s Field AVIRIS-NG Scaled Band Area and SNOTEL relationship**

The temporal temperature and effective grain radius comparison (Figure 8) is indicative of the relationship between snow albedo decay and ablation. As temperatures overall increased from 11 April to 1 May, effective grain radius increased. As shown in Wiscombe & Warren (1980) and Skiles & Painter (2017), an increase in effective grain radius translates to a decrease in snow albedo, and further accelerating snow melt due in part to increases in temperature and changing snow grain properties.

## **5.2. Error Analysis**

### **5.2.1. Sources of Possible Measurement Error**

Measurements were made in a standardized manner, but we acknowledge that there are minor differences that contribute to possible measurement error. For ground-

based measurements, these include the measurement height, angular orientation of the instrument foreoptic, illumination conditions, and non-snow materials in the field of view. Cold temperatures can also decrease instrument performance. All ground-based measurements were acquired at a height of approximately 1 m above the snow surface. Since the instrument and foreoptic are transported by individuals, it is challenging to confirm that all measurements were taken from the same height from snow or ground surface across all transects. All downward-pointing field spectrometer measurements were made with an approximate viewing zenith angle of  $0^\circ$  (as estimated using a bubble level), but handheld measurements will vary. These measurements were acquired in full sun, over unshaded snow (for the open and burned sites), and either full shade or full sun in the forested sites (no dappled illumination) but illumination conditions could vary slightly. Where Spectralon™ measurements were made, we assumed that the reflectance panel was level using a bubble level, but this could vary slightly. We also assumed that the field of view for all downward-pointing measurements contained only snow. For upward-pointing measurements, we assumed that any vegetation or people in the field of view would not significantly impact the measurements. These field of view effects could be significant in areas where trees are nearby. If the upward-pointing measurement contains tree canopy or spectrometer-operator effects, the incoming sunlight is attenuated, and the irradiance is affected by non-snow reflectance. If the downward-pointing measurement has vegetation or a spectrometer-operator in the field of view, this will decrease that measurement as well. This can introduce uncertainty in field spectrometer measurements of reflectance and albedo.

For all measurements, we assume that the snow surface is smooth. However, in some cases, there was surface roughness at the scale of 1-10 cm, mainly due to wind and localized melt due to forest litter on the snow surface. The impact of a surface roughness would be to reduce the magnitude of reflectance and albedo values due to the presence of small shadows on the snow surface. For the AVIRIS-NG and Landsat 8-9 OLI instruments, we assumed that the measurement geometry was nadir-looking (a viewing zenith angle of  $0^\circ$ ). Differences in viewing zenith can have a slight impact on reflectance and depends on illumination angle, local topography, and local surface roughness.

### **5.2.2. Atmospheric Correction**

Atmospheric correction was performed by the JPL AVIRIS-NG image processing team. Because there were no direct measurements of atmospheric characteristics, the team used a standard atmospheric profile for the correction, which may have over-corrected some reflectance values. This would be especially obvious in the visible part of the spectrum, where atmospheric scattering is greatest.

### **5.2.3. Illumination Conditions**

Illuminations conditions, such as clouds, low sun angle, shadows, surface roughness, topographic variability and mixed pixels, affect accuracy of snow albedo measurements. To minimize effects of varying solar zenith angle, all measurements were taken within two hours of solar noon. Ground and airborne measurements were only collected and analyzed if clear sky conditions existed. However, in some cases there were high thin cirrus clouds present, but not blocking the solar beam. Subvisual cirrus clouds might have been present

but without measurements of atmospheric spectral transmittance, it is not possible to characterize and remove such effects.

#### **5.2.4. Spectral Mixtures**

Data acquired by AVIRIS-NG and Landsat will include more than one spectral endmember. Uncertainty in the number of endmembers increases as the field of view increases. All ground-based measurements that are compared to airborne and satellite data are assumed to only include snow. However, there is always the possibility that changing lightning conditions and human interference may have impacted the field spectrometer, ground-based data. As the field of view increases, we assume all AVIRIS-NG and Landsat pixels are mixed. These assumptions are what led to the linear spectral unmixing analysis.

## **6. CONCLUSIONS**

This research provides a detailed comparison of hyperspectral and multispectral snow and landscape albedo values across spatial scales from centimeters to tens of meters using ground-based, airborne, and satellite-based sensors in the Alaskan boreal forest. Our goal was to develop a better understanding of variations in snow albedo indifferent landscapes including open, burned, and unburned forested areas.

We found that snow surface reflectance measurements vary depending on the spatial resolution of the observation and this is influenced by the fraction of vegetation in the ground-instantaneous field of view. In open areas, AVIRIS-NG data are in good agreement with ground-based spectrometer measurements. Areas with vegetation, such as the burned and forested sites require spectral unmixing of pixels to identify snow covered

areas and quantify the vegetation fraction in a pixel. As the spatial resolution decreases, the mixed pixel effect introduces greater uncertainty. One of our key findings is that albedo and reflectance at the landscape scale decrease linearly with increasing vegetation fraction in a pixel. This linear relationship is evident in both the visible and near-infrared wavelengths. While this study is limited in temporal and spatial scope, it provides an important preliminary understanding that can be more widely applied and evaluated. To fully quantify this landscape albedo versus snow albedo question, future work can build on these initial results by examining a wider range of vegetation types, snow conditions (patchy vs. continuous; dirty vs. clean), and illumination conditions (shadows, clouds).

The NASA SnowEx Snow Albedo 2023 campaign brought together scientists from multiple different universities and agencies. While the field methods were standardized to the best of participants abilities for this specific effort, it is apparent that the snow science community would benefit greatly from standardized field practices. Specific efforts will require methods to align with the project objectives, however general standardized practices decrease uncertainties that arise when comparing studies.

As temperatures continue to increase with anthropogenic climate change, we expect a shorter snow cover season and increases in wildfire activity in the Alaskan Boreal Forest and the western United States. As fires further expand into the seasonal snow zone, this will affect snow and landscape albedo and influence snowmelt patterns and rates. The timeframe of these impacts on downstream water resource quantity, quality and timing remains unknown and is an area of future research. Current ecohydrology and water resource models oversimplify snow albedo and how it changes over the course of the snow season and over years since fire occurrence. For instance, at the point scale, forest litter and

black carbon on the snow surface increase in recently burned forests. Over time, post-fire carbon deposition decreases, and snow albedo increases as burned trees fall or no longer shed charred material. If the forest doesn't grow back, or if it does so very slowly, the post-fire snow albedo may recover to the point that it is even higher than pre-fire conditions since forest litter is not accumulating on the snowpack surface. At the landscape scale, the post-fire albedo starts out high but over time, as the forest regrows, the landscape albedo will decline as a function of forest density. In burned areas, we need long-term studies of snow and landscape albedo in conjunction with rates of black carbon and burned woody debris shedding, forest regrowth, and forest litter deposition. Moreover, we seek to further evaluate the linear relationship between landscape albedo and vegetation fractions for a wide range of forest types in burned and unburned forests. We also encourage future research to incorporate UAS to bridge the spatial resolution gap between ground and airborne snow surface reflectance.

## REFERENCES

- Adams, J. B., Smith, M. O., & Johnson, P. E. (1986). Spectral mixture modeling: A new analysis of rock and soil types at the Viking Lander 1 Site. *Journal of Geophysical Research: Solid Earth*, 91(B8), 8098–8112. <https://doi.org/10.1029/JB091iB08p08098>
- Alizadeh, M. R., Abatzoglou, J. T., Luce, C. H., Adamowski, J. F., Farid, A., & Sadegh, M. (2021). Warming enabled upslope advance in western US forest fires. *Proceedings of the National Academy of Sciences*, 118(22), e2009717118. <https://doi.org/10.1073/pnas.2009717118>
- Amaral, T., Wake, C. P., Dibb, J. E., Burakowski, E. A., & Stampone, M. (2017). A simple model of snow albedo decay using observations from the Community Collaborative Rain, Hail, and Snow-Albedo (CoCoRaHS-Albedo) Network. *Journal of Glaciology*, 63(241), 877–887. <https://doi.org/10.1017/jog.2017.54>
- AVIRIS - Airborne Visible / Infrared Imaging Spectrometer - Data. (n.d.). <https://aviris.jpl.nasa.gov/data/newdata.html>
- Barnett, T. P., Adam, J. C., & Lettenmaier, D. P. (2005). Potential impacts of a warming climate on water availability in snow-dominated regions. *Nature*, 438(7066), 303–309. <https://doi.org/10.1038/nature04141>
- Betts, A. K., & Ball, J. H. (1997). Albedo over the boreal forest. *Journal of Geophysical Research: Atmospheres*, 102(D24), 28901–28909. <https://doi.org/10.1029/96JD03876>
- Bhattacharya, B. K., Green, R. O., Rao, S., Saxena, M., Sharma, S., Kumar, K. A., Srinivasulu, P., Sharma, S., Dhar, D., Bandyopadhyay, S., Bhatwadekar, S., & Kumar, R. (2019). An overview of AVIRIS-NG airborne hyperspectral science campaign over India. *Current Science*, 116(7), 1082–1088. <https://www.jstor.org/stable/27138000>
- Calvin, K., Dasgupta, D., Krinner, G., Mukherji, A., Thorne, P. W., Trisos, C., Romero, J., Aldunce, P., Barrett, K., Blanco, G., Cheung, W. W. L., Connors, S., Denton, F., Diongue-Niang, A., Dodman, D., Garschagen, M., Geden, O., Hayward, B., Jones, C., ... Péan, C. (2023). *IPCC, 2023: Climate Change 2023: Synthesis Report. Contribution of Working Groups I, II and III to the Sixth Assessment Report of the Intergovernmental Panel on Climate Change [Core Writing Team, H. Lee and J. Romero (eds.)]*. IPCC, Geneva, Switzerland. <https://doi.org/10.59327/IPCC/AR6-9789291691647>
- Chapman, J. W., Thompson, D. R., Helmlinger, M. C., Bue, B. D., Green, R. O., Eastwood, M. L., Geier, S., Olson-Duvall, W., & Lundeen, S. R. (2019). Spectral and Radiometric Calibration of the Next Generation Airborne Visible Infrared Spectrometer (AVIRIS-NG). *Remote Sensing*, 11(18), 2129. <https://doi.org/10.3390/rs11182129>
- Delaney, I., Kaspari, S., & Jenkins, M. (2015). Black carbon concentrations in snow at Tronsen Meadow in Central Washington from 2012 to 2013: Temporal and spatial variations and the role of local forest fire activity. *Journal of Geophysical Research: Atmospheres*, 120(18), 9160–9172. <https://doi.org/10.1002/2015JD023762>
- Donahue, C., Skiles, S. M., & Hammonds, K. (2021). In situ effective snow grain size mapping using a compact hyperspectral imager. *Journal of Glaciology*, 67(261), 49–57. <https://doi.org/10.1017/jog.2020.68>
- Earth Resources Observation And Science (EROS) Center. (2013). *Collection-2 Landsat 8-9 OLI (Operational Land Imager) and TIRS (Thermal Infrared Sensor) Level-2 Science Products*. U.S. Geological Survey. <https://doi.org/10.5066/P90GBGM6>

- Fassnacht, S. R., Williams, M. W., & Corrao, M. V. (2009). Changes in the surface roughness of snow from millimetre to metre scales. *Ecological Complexity*, 6(3), 221–229. <https://doi.org/10.1016/j.ecocom.2009.05.003>
- Games Howell Post-hoc Tests* — *games\_howell\_test*. (n.d.). [https://rpkg.sdatanovia.com/rstatix/reference/games\\_howell\\_test.html](https://rpkg.sdatanovia.com/rstatix/reference/games_howell_test.html)
- Gersh, M., Gleason, K. E., & Surunis, A. (2022). Forest Fire Effects on Landscape Snow Albedo Recovery and Decay. *Remote Sensing*, 14(16), 4079. <https://doi.org/10.3390/rs14164079>
- Gleason, K. E., McConnell, J. R., Arienzo, M. M., Chellman, N., & Calvin, W. M. (2019). Four-fold increase in solar forcing on snow in western U.S. burned forests since 1999. *Nat Commun*, 10(1), 2026. <https://doi.org/10.1038/s41467-019-09935-y>
- Gleason, K. E., & Nolin, A. W. (2016). Charred forests accelerate snow albedo decay: parameterizing the post-fire radiative forcing on snow for three years following fire. *Hydrological Processes*, 30(21), 3855–3870. <https://doi.org/10.1002/hyp.10897>
- Gleason, K. E., Nolin, A. W., & Roth, T. R. (2013). Charred forests increase snowmelt: Effects of burned woody debris and incoming solar radiation on snow ablation. *Geophysical Research Letters*, 40(17), 4654–4661. <https://doi.org/10.1002/grl.50896>
- Hale, K. E., Jennings, K. S., Musselman, K. N., Livneh, B., & Molotch, N. P. (2023). Recent decreases in snow water storage in western North America. *Commun Earth Environ*, 4(1), 1–11. <https://doi.org/10.1038/s43247-023-00751-3>
- Hammond, J. C., Saavedra, F. A., & Kampf, S. K. (2018). Global snow zone maps and trends in snow persistence 2001–2016. *International Journal of Climatology*, 38(12), 4369–4383. <https://doi.org/10.1002/joc.5674>
- Hao, D., Bisht, G., He, C., Bair, E., Huang, H., Dang, C., Rittger, K., Gu, Y., Wang, H., Qian, Y., & Leung, L. R. (2022). *Improving snow albedo modeling in E3SM land model (version 2.0) and assessing its impacts on snow and surface fluxes over the Tibetan Plateau*. <https://doi.org/10.5194/gmd-2022-67>
- Hatchett, B. J., Koshkin, A. L., Guirguis, K., Rittger, K., Nolin, A. W., Heggli, A., Rhoades, A. M., East, A. E., Siirila-Woodburn, E. R., Brandt, W. T., Gershunov, A., & Haleakala, K. (2023). Midwinter Dry Spells Amplify Post-Fire Snowpack Decline. *Geophysical Research Letters*, 50(3), e2022GL101235. <https://doi.org/10.1029/2022GL101235>
- Higuera, P. E., Abatzoglou, J. T., Littell, J. S., & Morgan, P. (2015). The Changing Strength and Nature of Fire-Climate Relationships in the Northern Rocky Mountains, U.S.A., 1902–2008. *PLOS ONE*, 10(6), e0127563. <https://doi.org/10.1371/journal.pone.0127563>
- Letcher, T. W., & Minder, J. R. (2015). Characterization of the Simulated Regional Snow Albedo Feedback Using a Regional Climate Model over Complex Terrain. *Journal of Climate*, 28(19), 7576–7595. <https://doi.org/10.1175/JCLI-D-15-0166.1>
- Marlon, J. R., Bartlein, P. J., Gavin, D. G., Long, C. J., Anderson, R. S., Briles, C. E., Brown, K. J., Colombaroli, D., Hallett, D. J., Power, M. J., Scharf, E. A., & Walsh, M. K. (2012). Long-term perspective on wildfires in the western USA. *Proceedings of the National Academy of Sciences*, 109(9), E535–E543. <https://doi.org/10.1073/pnas.1112839109>
- Matzl, M., & Schneebeli, M. (2006). Measuring specific surface area of snow by near-infrared photography. *Journal of Glaciology*, 52(179), 558–564. <https://doi.org/10.3189/172756506781828412>

- Mote, P. W., Hamlet, A. F., Clark, M. P., & Lettenmaier, D. P. (2005). DECLINING MOUNTAIN SNOWPACK IN WESTERN NORTH AMERICA\*. *Bulletin of the American Meteorological Society*, 86(1), 39–50. <https://doi.org/10.1175/BAMS-86-1-39>
- Mote, P. W., Li, S., Lettenmaier, D. P., Xiao, M., & Engel, R. (2018). Dramatic declines in snowpack in the western US. *Npj Clim Atmos Sci*, 1(1), 1–6. <https://doi.org/10.1038/s41612-018-0012-1>
- Musselman, K. N., Clark, M. P., Liu, C., Ikeda, K., & Rasmussen, R. (2017). Slower snowmelt in a warmer world. *Nature Clim Change*, 7(3), 214–219. <https://doi.org/10.1038/nclimate3225>
- Nicolas Zuanon. (2013). IceCube, a portable and reliable instrument for snow specific surface area measurement in the field. *International Snow Science Workshop Grenoble “Chamonix Mont-Blanc”*.
- Nolin, A. W., & Dozier, J. (2000). A Hyperspectral Method for Remotely Sensing the Grain Size of Snow. *Remote Sensing of Environment*, 74(2), 207–216. [https://doi.org/10.1016/S0034-4257\(00\)00111-5](https://doi.org/10.1016/S0034-4257(00)00111-5)
- Nolin, A. W., Sproles, E. A., Rupp, D. E., Crumley, R. L., Webb, M. J., Palomaki, R. T., & Mar, E. (2021). New snow metrics for a warming world. *Hydrological Processes*, 35(6), e14262. <https://doi.org/10.1002/hyp.14262>
- O’Halloran, T. L., Acker, S. A., Joerger, V. M., Kertis, J., & Law, B. E. (2014). Postfire influences of snag attrition on albedo and radiative forcing. *Geophysical Research Letters*, 41(24), 9135–9142. <https://doi.org/10.1002/2014GL062024>
- Painter, T. H., Roberts, D. A., Green, R. O., & Dozier, J. (1998). The Effect of Grain Size on Spectral Mixture Analysis of Snow-Covered Area from AVIRIS Data. *Remote Sensing of Environment*, 65(3), 320–332. [https://doi.org/10.1016/S0034-4257\(98\)00041-8](https://doi.org/10.1016/S0034-4257(98)00041-8)
- Parks, S. A., Miller, C., Parisien, M.-A., Holsinger, L. M., Dobrowski, S. Z., & Abatzoglou, J. (2015). Wildland fire deficit and surplus in the western United States, 1984–2012. *Ecosphere*, 6(12), 1–13. <https://doi.org/10.1890/ES15-00294.1>
- R Core Team. (2023). *R: A Language and Environment for Statistical Computing*. R Foundation for Statistical Computing.
- Randerson, J. T., Liu, H., Flanner, M. G., Chambers, S. D., Jin, Y., Hess, P. G., Pfister, G., Mack, M. C., Treseder, K. K., Welp, L. R., Chapin, F. S., Harden, J. W., Goulden, M. L., Lyons, E., Neff, J. C., Schuur, E. A. G., & Zender, C. S. (2006). The Impact of Boreal Forest Fire on Climate Warming. *Science*, 314(5802), 1130–1132. <https://doi.org/10.1126/science.1132075>
- Rittger, K., Painter, T. H., & Dozier, J. (2013). Assessment of methods for mapping snow cover from MODIS. *Advances in Water Resources*, 51, 367–380. <https://doi.org/10.1016/j.advwatres.2012.03.002>
- Robinson, D. A., & Frei, A. (2000). Seasonal Variability of Northern Hemisphere Snow Extent Using Visible Satellite Data. *The Professional Geographer*, 52(2), 307–315. <https://doi.org/10.1111/0033-0124.00226>
- Schaepman-Strub, G., Schaepman, M. E., Painter, T. H., Dangel, S., & Martonchik, J. V. (2006). Reflectance quantities in optical remote sensing—definitions and case studies. *Remote Sensing of Environment*, 103(1), 27–42. <https://doi.org/10.1016/j.rse.2006.03.002>
- Seidel, F. C., Rittger, K., Skiles, S. M., Molotch, N. P., & Painter, T. H. (2016). Case study of spatial and temporal variability of snow cover, grain size, albedo and radiative forcing in the Sierra Nevada and Rocky Mountain snowpack derived from imaging

- spectroscopy. *The Cryosphere*, 10(3), 1229–1244. <https://doi.org/10.5194/tc-10-1229-2016>
- Skiles, S. M., Donahue, C. P., Hunsaker, A. G., & Jacobs, J. M. (2023). UAV hyperspectral imaging for multiscale assessment of Landsat 9 snow grain size and albedo. *Frontiers in Remote Sensing*, 3. <https://www.frontiersin.org/articles/10.3389/frsen.2022.1038287>
- Skiles, S. M., & Painter, T. (2017). Daily evolution in dust and black carbon content, snow grain size, and snow albedo during snowmelt, Rocky Mountains, Colorado. *Journal of Glaciology*, 63(237), 118–132. <https://doi.org/10.1017/jog.2016.125>
- Smith, C. W., Panda, S. K., Bhatt, U. S., & Meyer, F. J. (2021). Improved Boreal Forest Wildfire Fuel Type Mapping in Interior Alaska Using AVIRIS-NG Hyperspectral Data. *Remote Sensing*, 13(5), 897. <https://doi.org/10.3390/rs13050897>
- Smoot, E. E., & Gleason, K. E. (2021). Forest Fires Reduce Snow-Water Storage and Advance the Timing of Snowmelt across the Western U.S. *Water*, 13(24), 3533. <https://doi.org/10.3390/w13243533>
- Spectralon® Diffuse Reflectance Targets - Durable Reflectance Panels. (n.d.). In *Labsphere*. <https://www.labsphere.com/product/spectralon-reflectance-targets/>
- Stevens, J. T. (2017). Scale-dependent effects of post-fire canopy cover on snowpack depth in montane coniferous forests. *Ecological Applications*, 27(6), 1888–1900. <https://doi.org/10.1002/eap.1575>
- Stewart, I. T., Cayan, D. R., & Dettinger, M. D. (2005). Changes toward Earlier Streamflow Timing across Western North America. *Journal of Climate*, 18(8), 1136–1155. <https://doi.org/10.1175/JCLI3321.1>
- Thackeray, C. W., & Fletcher, C. G. (2016). Snow albedo feedback: Current knowledge, importance, outstanding issues and future directions. *Progress in Physical Geography: Earth and Environment*, 40(3), 392–408. <https://doi.org/10.1177/0309133315620999>
- Thompson, D. R., Natraj, V., Green, R. O., Helmlinger, M. C., Gao, B.-C., & Eastwood, M. L. (2018). Optimal estimation for imaging spectrometer atmospheric correction. *Remote Sensing of Environment*, 216, 355–373. <https://doi.org/10.1016/j.rse.2018.07.003>
- Traversa, G., Fugazza, D., Senese, A., & Frezzotti, M. (2021). Landsat 8 OLI Broadband Albedo Validation in Antarctica and Greenland. *Remote Sensing*, 13(4), 799. <https://doi.org/10.3390/rs13040799>
- United States. Army. Corps of Engineers. (1956). *Snow hydrology: Summary report of the snow investigations*.
- U.S. Geological Survey. (2012). *EarthExplorer*.
- Warren, S. G. (1982). Optical properties of snow. *Reviews of Geophysics*, 20(1), 67–89. <https://doi.org/10.1029/RG020i001p00067>
- Warren, S. G., & Wiscombe, W. J. (1980). A Model for the Spectral Albedo of Snow. II: Snow Containing Atmospheric Aerosols. *Journal of the Atmospheric Sciences*, 37(12), 2734–2745. [https://doi.org/10.1175/1520-0469\(1980\)037<2734:AMFTSA>2.0.CO;2](https://doi.org/10.1175/1520-0469(1980)037<2734:AMFTSA>2.0.CO;2)
- Westerling, A. L. (2016). Increasing western US forest wildfire activity: sensitivity to changes in the timing of spring. *Philosophical Transactions of the Royal Society B: Biological Sciences*, 371(1696), 20150178. <https://doi.org/10.1098/rstb.2015.0178>

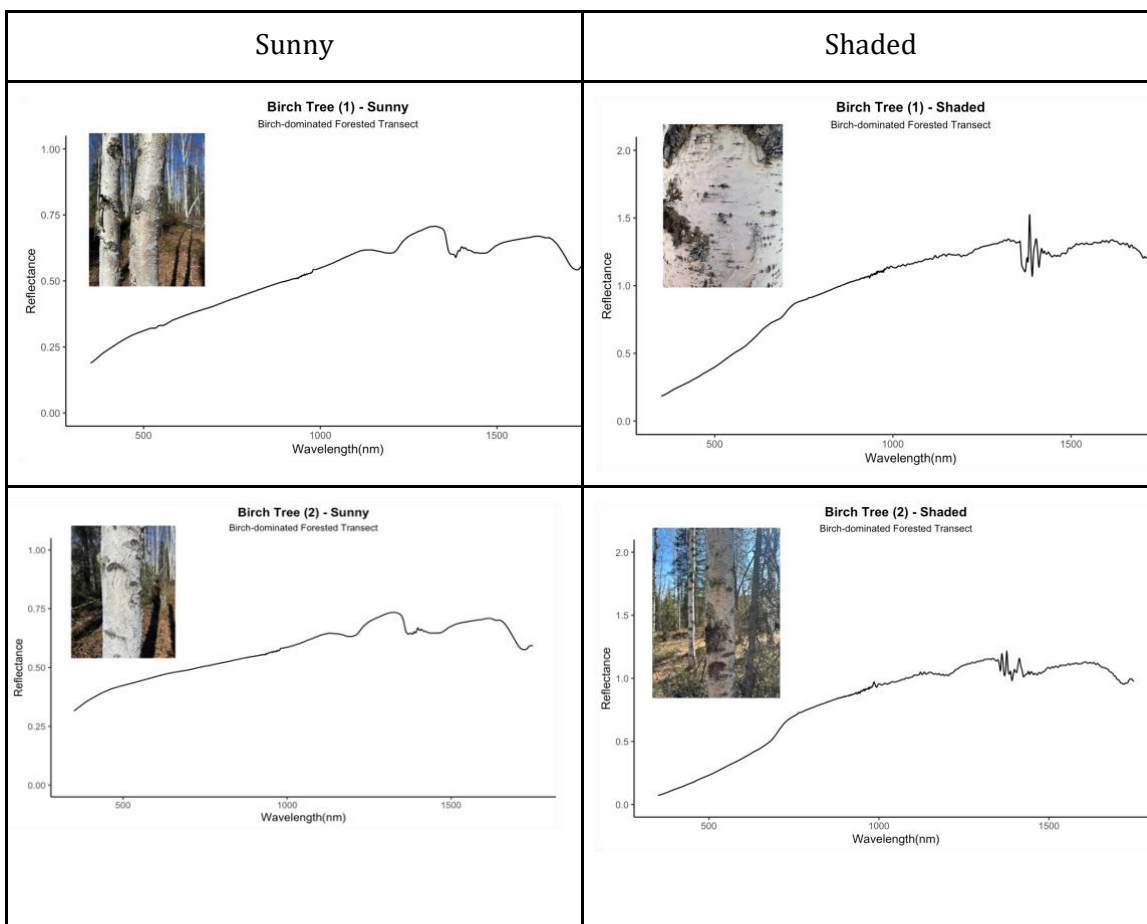
- Westerling, A. L., Hidalgo, H. G., Cayan, D. R., & Swetnam, T. W. (2006). Warming and Earlier Spring Increase Western U.S. Forest Wildfire Activity. *Science*, *313*(5789), 940–943.  
<https://doi.org/10.1126/science.1128834>
- Wiscombe, W. J., & Warren, S. G. (1980). A Model for the Spectral Albedo of Snow. I: Pure Snow. *Journal of the Atmospheric Sciences*, *37*(12), 2712–2733.  
[https://doi.org/10.1175/1520-0469\(1980\)037<2712:AMFTSA>2.0.CO;2](https://doi.org/10.1175/1520-0469(1980)037<2712:AMFTSA>2.0.CO;2)
- Zolles, T., & Born, A. (2021). Sensitivity of the Greenland surface mass and energy balance to uncertainties in key model parameters. *The Cryosphere*, *15*(6), 2917–2938.  
<https://doi.org/10.5194/tc-15-2917-2021>

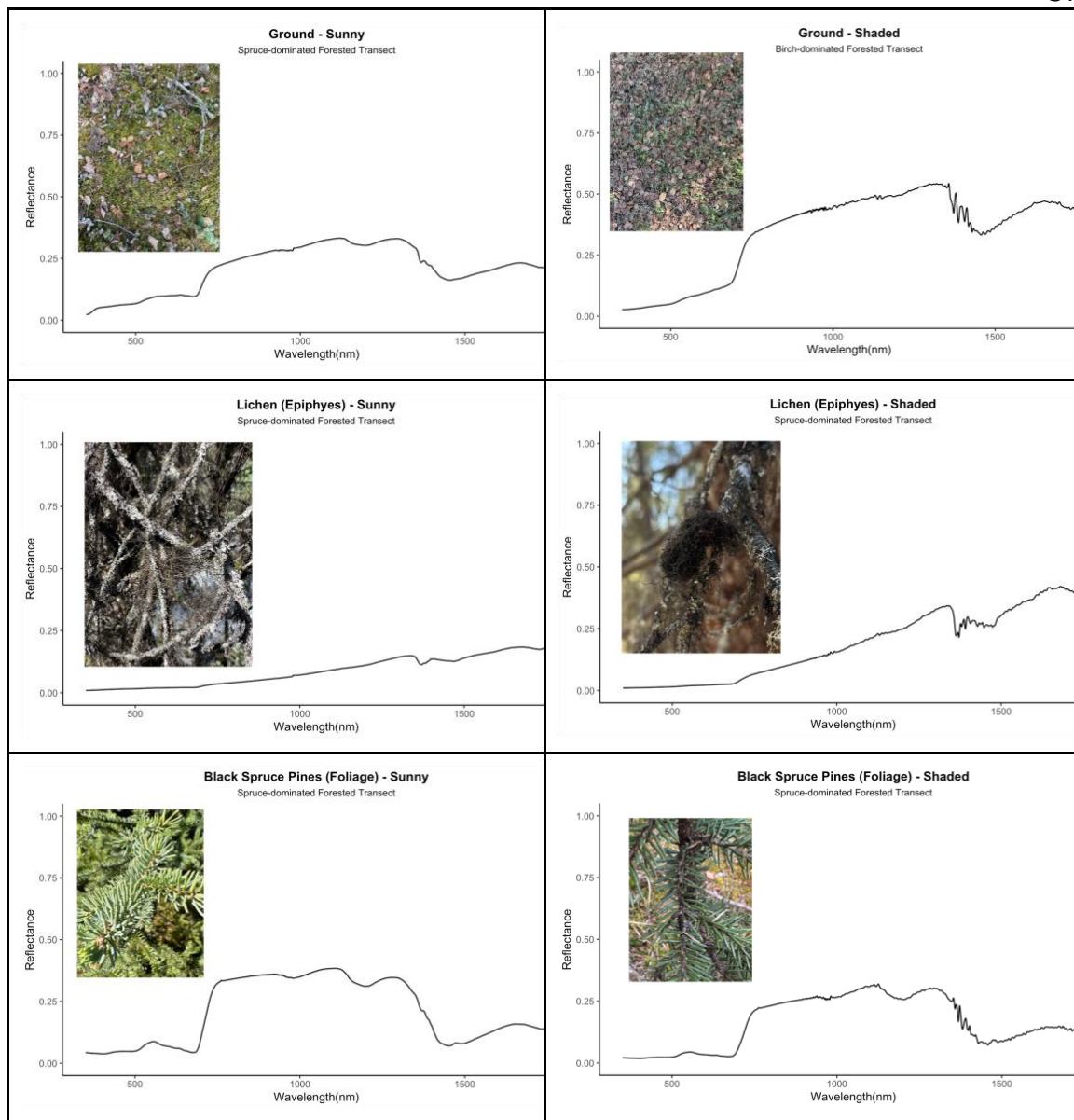
## SUPPLEMENTAL MATERIAL

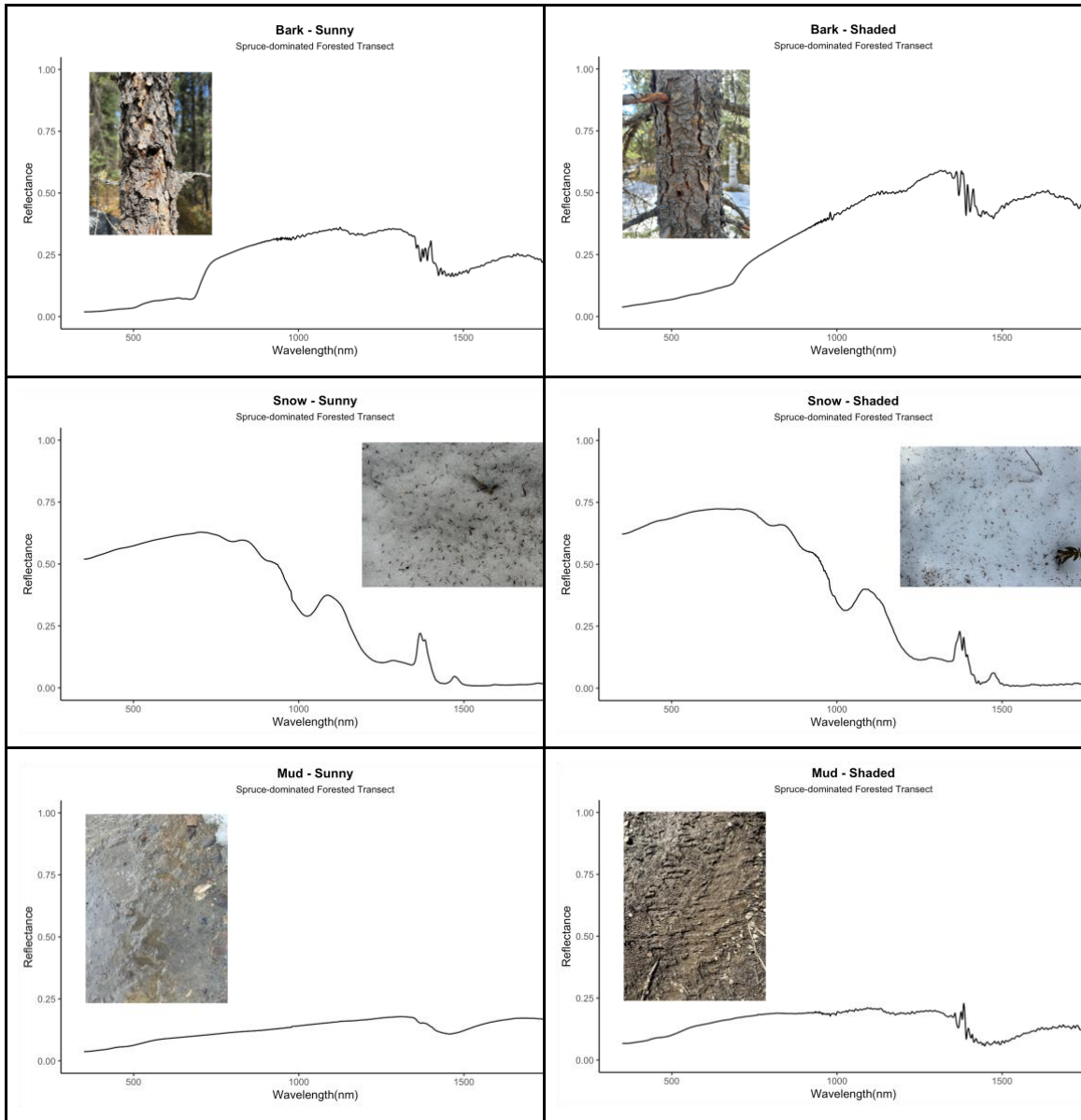
## DATA AND CODE AVAILABILITY

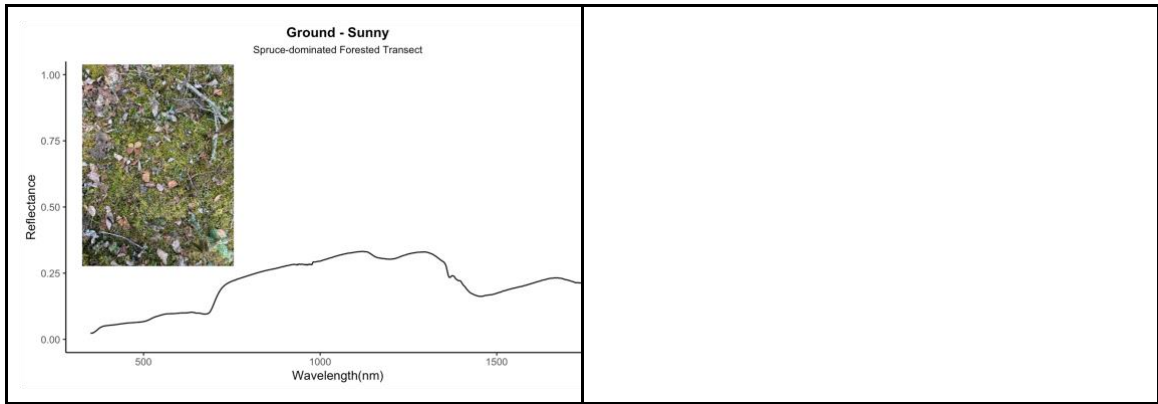
All field spectrometer and AVIRIS-NG data is available for download through the NSIDC website as part of the SnowEx campaign (<https://nsidc.org/data/snowex>). The code used in this research is available here: <https://doi.org/10.5061/dryad.7m0cfxq43>

## SPECTRAL LIBRARY









## TABLES

**Table S.1.** Average measured reflectance values for ground-based field spectrometer and Landsat 8-9. Field spectrometer spectral bands were aggregated to Landsat 8-9 spectral resolution. Measurements are shown only for near-coincident ground-based measurements and Landsat overpasses occurred ( $\pm 1$  day).

Average Reflectance Aggregated to Landsat Band Spectral Range								
Field Spectrometer								
Location	Delta Junction					CPCRW		
Date	13 April 2023		20 April 2023			19 April 2023		
Transect	T1	T2	T1	T2	T3	T1	T2	T3
Band	Open	Forest	Open	Forest	Open	Burned	Forest	Open
Band 1	0.98	1.16	1.03	0.99	0.95	0.97	1.01	1.07
Band 2	0.97	1.18	1.01	0.98	0.94	0.96	1.00	1.06
Band 3	0.96	1.20	0.98	0.96	0.93	0.95	0.98	1.04
Band 4	0.93	1.20	0.94	0.92	0.90	0.92	0.95	1.01
Band 5	0.84	1.12	0.82	0.79	0.78	0.79	0.82	0.91
Band 6	0.12	0.18	0.07	0.06	0.07	0.09	0.05	0.10
Band 7	0.14	0.22	0.08	0.07	0.08	0.09	0.05	0.10
Landsat 8-9 OLI								
Band 1	1.00	0.40	0.85	0.62	0.83	0.67	0.56	0.67
Band 2	1.02	0.39	0.86	0.61	0.83	0.68	0.57	0.66
Band 3	0.96	0.38	0.80	0.57	0.78	0.65	0.55	0.60
Band 4	0.97	0.36	0.79	0.55	0.76	0.66	0.55	0.59
Band 5	0.89	0.43	0.69	0.54	0.68	0.61	0.55	0.54
Band 6	0.11	0.06	0.11	0.10	0.10	0.09	0.06	0.04
Band 7	0.13	0.07	0.11	0.10	0.10	0.10	0.06	0.05

**Table S.2.** Reference table including location input to NOAA Solar Position Calculator and estimates solar zenith angle.

<b>Transect Location and Solar Zenith Angle</b>				
<b>Transect</b>	<b>Latitude</b>	<b>Longitude</b>	<b>Date</b>	<b>SZA</b>
CARI_T1_0407	65.1599	-147.613	7-Apr	58.8
CARI_T2_0407	65.1554	-147.504	7-Apr	58.8
DEJU_T1_0413	63.8876	-145.763	13-Apr	55.4
DEJU_T2_0413	63.8817	-145.753	13-Apr	55.4
CARI_T1_0414	65.1599	147.613	14-Apr	56.4
CRMF_T1_0415	64.8661	-147.727	15-Apr	56.2
CARI_T1_0419	65.1599	-147.613	19-Apr	55.6
CARI_T2_0419	65.1554	-147.504	19-Apr	54.5
CARI_T3_0419	65.1541	-147.476	19-Apr	54.5
DEJU_T1_0420	63.8876	-145.763	20-Apr	52.9
DEJU_T2_0420	63.8817	-145.753	20-Apr	52.9
DEJU_T3_0420	63.863	145.726	20-Apr	52.9
<b>Average Solar Zenith Angle</b>				<b>55.2</b>

**Table S.3.** Look up table using SNICAR modeled snow spectra with parameters previously discussed at various effective grain radii.

<b>Effective Grain Radius Lookup Table</b>	
Effective Grain Radius (microns)	Scaled Band Area
50	0.289
75	0.350
100	0.401
200	0.558
300	0.675
400	0.771
450	0.814
500	0.854
550	0.891
600	0.927
650	0.961
700	0.993
750	1.024
800	1.054
850	1.082
900	1.109
950	1.136
1000	1.161
1050	1.186
1150	1.233
1250	1.277
1350	1.319
1450	1.359
1500	1.378

## FIGURES

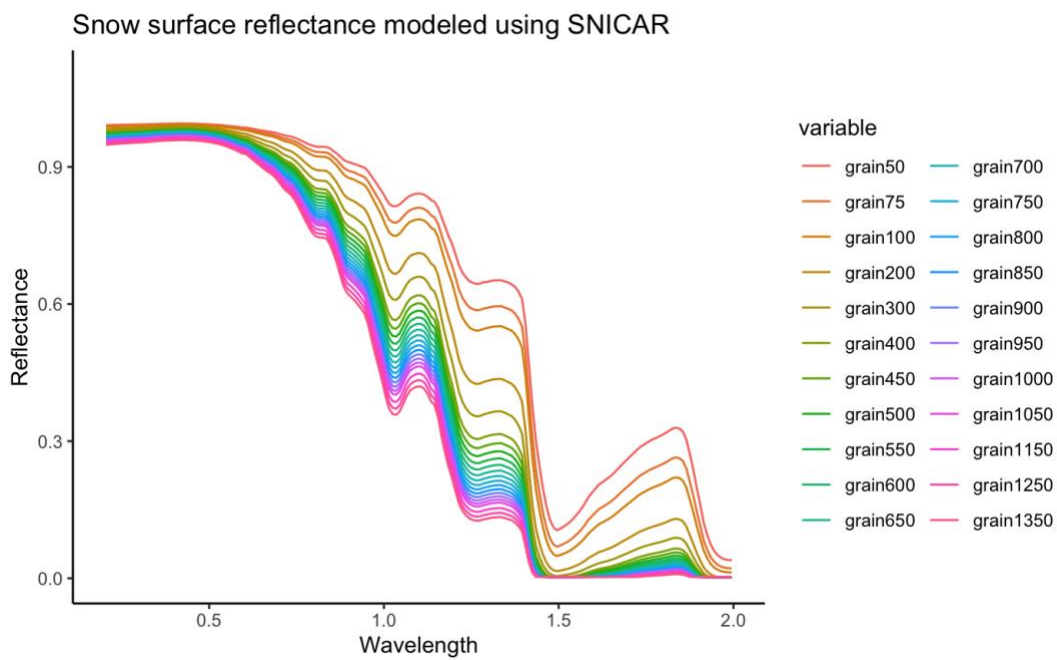


**Figure S.1.** SNICAR modeled snow surface reflectance using range of snow grain effective radius values. Grain radii values are in units of microns.

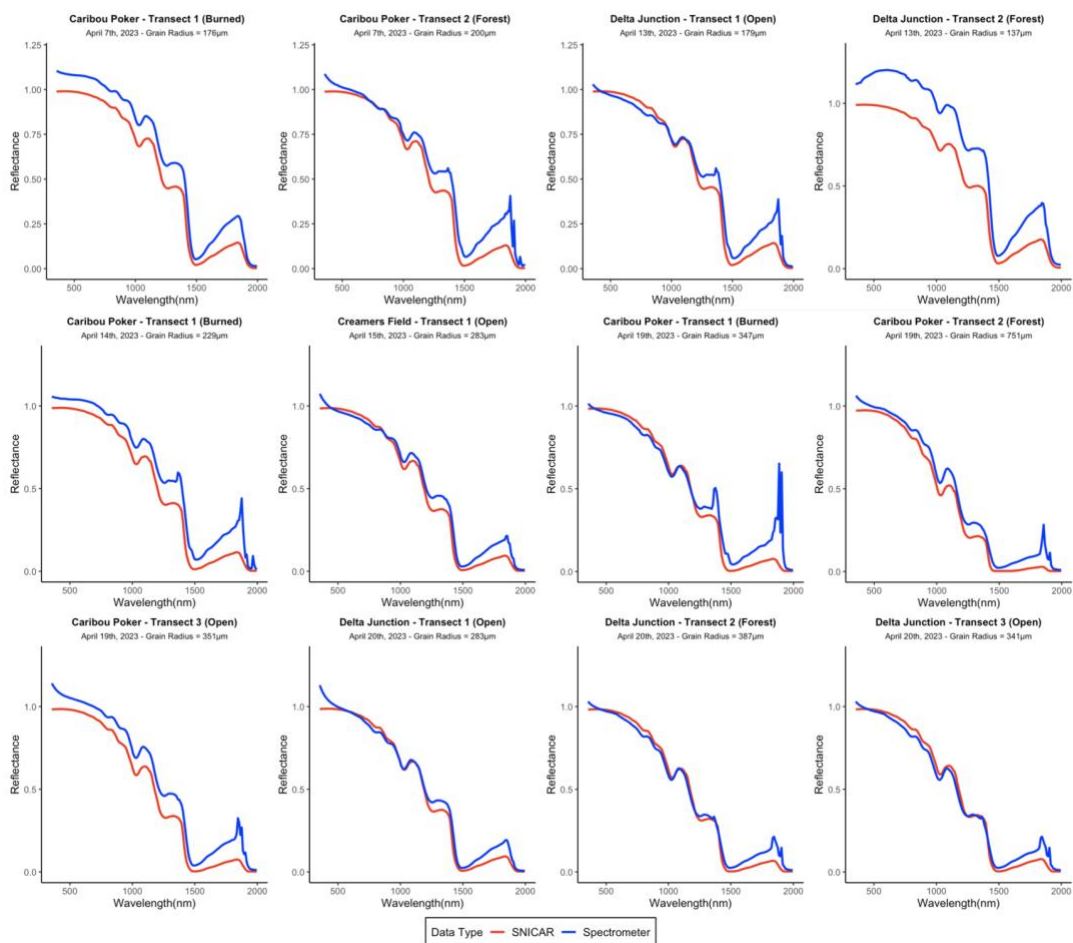


**Figure S.2.** Spectral comparison between field spectrometer measurements and modeled SNICAR spectra whose effective grain radius was set to that of the *in situ* measurement.

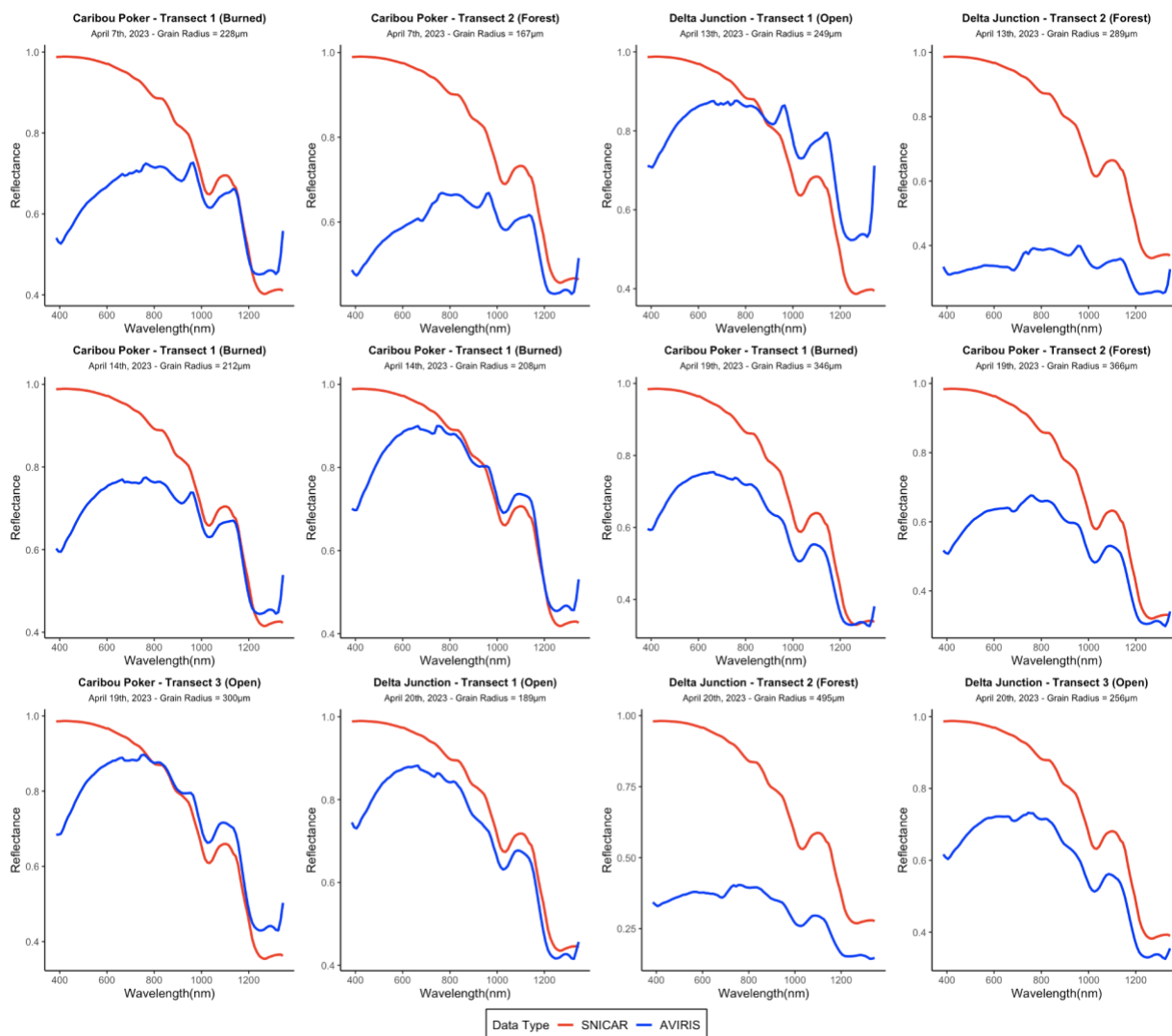


**Figure S.3.** Spectral comparison between AVIRIS-NG measurements and modeled SNICAR spectra whose effective grain radius was set to that of the *in situ* measurement.